Invited review article

Driving forces of mineral recrystallization in aqueous solutions derived from kinetic modeling of isotope exchange data

Enzo Curti [a,*], Jan Tits [a], Frank Heberling [b]

[a] *Laboratory for Waste Management, Paul Scherrer Institute, Forschungsstrasse 111, Villigen PSI CH-5232, Switzerland*
[b] *Institute for Nuclear Waste Disposal, Karlsruhe Institute of Technology, 76021 Karlsruhe, Germany*

ARTICLE INFO

ABSTRACT

Recrystallization in aqueous solutions is a ubiquitous process susceptible to control the entrapment and release of toxic contaminants in the subsurface. However, unraveling the underlying mechanisms and driving forces has proven to be elusive, as recrystallization frequently follows different kinetic pathways even for the same mineral, depending on its initial state and pre-treatment. To obtain a better insight, a large body of experimental data from isotope tracer experiments carried out in the past two decades on a variety of minerals (baryte, calcite, calcium-silicate hydrates, goethite, and UO_2) was reviewed and modeled, using the HOmogeneous Recrystallization (HOR) and the Continuous HOmogeneous Recrystallization (CHOR) models, both coupled to instantaneous reversible adsorption and denoted as a whole as C(HOR)-K_d models.

In the first part of this contribution, we develop the full mathematical formalism and discuss the model parameters. The second part is devoted to the review, modeling and interpretation of selected data. It is shown that the C(HOR)-K_d models successfully reproduce recrystallization data for widely different minerals, including Fe-isotope data on goethite modeled elsewhere using a different approach ("back-reaction" model). In combination with microscopic characterization data, the modeling results allow us to identify the thermodynamic driving forces controlling the recrystallization kinetics. These include: (i) the reduction of surface energy excess arising from a high density of defects (kink sites, dislocations, steps) and/or a high initial specific surface area; (ii) the spontaneous tendency to increase crystallinity (increase in crystallite size, transformation to a more stable habitus); (iii) the annealing of chemical potential gradients when foreign trace elements are incorporated as solid solution into the recrystallized solid; (iv) the annealing of electric potential gradients in redox active solids (Fe oxy-hydroxides). Our findings demonstrate that mineral recrystallization in aqueous solutions is a complex phenomenon driven by multiple mechanisms correlated to the properties of the primary solid. Accurate predictions on kinetics and extent of recrystallization are possible only after detailed characterization of the solid down to the molecular scale.

1. Introduction

Mineral formation and transformation in low-temperature earth environments (up to hydrothermal conditions) is generally governed by reactions in aqueous solutions (Weyl, 1959; Putnis, 2009; Ruiz-Agudo et al., 2014). If local conditions remain close to saturation equilibrium, a formerly precipitated mineral may undergo *isochemical, isostructural recrystallization* via dissolution/precipitation (D/P) reactions, e.g. during diagenesis of sedimentary rocks (Chanda and Fantle, 2017). Moreover, recrystallization may control the entrapment and release of dissolved trace elements (Frierdich and Catalano, 2011), playing a crucial role in

limiting the transport of hazardous contaminants. It is therefore imperative to understand its driving mechanisms and kinetics. Not considered in this paper are other types of isochemical mineral transformations, also usually termed "recrystallization" in the geological and metallurgical literature, occurring at high pressure-temperature conditions, e.g. in melts, during regional or contact metamorphism, or during rock deformation processes (Prior et al., 2004; Cross and Skemer, 2019).

Modeling recrystallization in time and space is a difficult task, particularly when coupled to solute transport in porous or fractured rocks. Once a mineral has nucleated, the subsequent precipitation and dissolution rates (in supersaturated and undersaturated solution,

respectively) may be predicted by applying affinity-based kinetic equations that depend linearly or with higher power (order) on the saturation index (Navrotsky, 2009; Putnis and Ruiz-Agudo, 2013; Bethke, 2022). Such "rate laws" are usually empirical and depend not only on saturation state (Busenberg and Plummer, 1986; Nagy and Lasaga, 1992; Lasaga, 2014), but also on chemical parameters such as *pH*, *Eh* or element ratios in solution (Pokrovsky and Schott, 2004; Zhang and Nancollas, 2014; Metz et al., 2023), on nucleation mechanisms (De Yoreo et al., 2015), biological activity (Hoffmann et al., 2021), the presence of inhibiting or catalyzing trace elements (Davis et al., 2000; De Yoreo et al., 2009; Nielsen et al., 2012; Bracco et al., 2012; Weber et al., 2018; Di Lorenzo et al., 2021; Camacho Meneses et al., 2025), mineral composition in solid solutions (Putnis and Putnis, 2007) and polymorphism (Di Lorenzo et al., 2019). Therefore, they are usually applicable only to a peculiar solid under restricted chemical conditions. On the atomistic scale, D/P kinetics was found to depend also on lattice defect distributions that can be described via stochastic approaches (Kurganskaya and Lüttge, 2024).

Recrystallization can be defined as a subset of D/P reactions without significant changes in the original chemical composition and atomic structure of the initial solid, occurring *at* or *close to* saturation equilibrium (Gorski and Fantle, 2017), the latter defined in terms of a thermodynamic solubility product, K_{sp}^0, of the recrystallizing mineral. The primary solid dissolves and re-precipitates in-situ into a slightly more stable form of the same mineral, under *quasi-constant* chemical conditions and mass conservation. Recrystallization in aqueous solutions is governed by the same principles as D/P reactions occurring in under/ supersaturated solutions, since they also involve local dissolution and re-precipitation, albeit usually at lower rates and – at the atomistic scale – through different mechanisms (Boistelle and Astier, 1988; Tsukamoto, 2016).

The term *quasi-constant* is deliberately chosen here to include small deviations from perfect saturation, which may arise from the slightly higher solubility induced by the high specific surface area of nanoparticulate solids, by abundant lattice defects on the mineral surface, or by unstable crystal habitus (Enüstün and Turkevich, 1960; Schindler, 1967; Heberling et al., 2016). In the case of nanoparticulate materials, the slightly enhanced solubility leads to dissolution and re-precipitation to less soluble (thermodynamically more stable) coarser particles, a process known as *Ostwald ripening,* in the classical definition of this term (Kahlweit, 1975; Tadros, 2013). A broader definition, not used here, also includes processes leading to a decrease in surface free energy without changes in particle size, e.g. the annealing of crystal defects or recrystallization to a more stable crystal habitus (Heberling et al., 2016; Sugimoto, 2019).

Quasi-constant saturation conditions also apply during recrystallization of a pure parent solid into a thermodynamically more stable dilute solid solution, when trace elements present in the aqueous phase are incorporated in specific lattice sites, e.g. Ra(II) and Sr(II) replacing Ba (II) in baryte. The variations in solubility induced by incorporation of these two elements have been identified to be the dominating driving force for the recrystallization of pure baryte into (Ra, Sr)-baryte (Vinograd et al., 2018a, 2018b; Brandt et al., 2015, 2020; Heberling et al., 2018; Weber et al., 2021).

McIntire (1963) formalized two popular models to describe empirically the entrapment of trace elements in a host mineral during co-precipitation. In the *homogeneous* partition model, the entire fraction of the trace element-bearing precipitated solid is in permanent equilibrium with the aqueous solution (see also Henderson and Kracek, 1927). In contrast, the *heterogeneous* partition model relies on the assumption that equilibrium between trace element in aqueous solution and co-precipitated solid is limited to a thin surface layer of the growing solid, while the previously incorporated (buried) trace element fraction remains inaccessible and is thus passivated. These two concepts were later adapted by Curti et al. (2005, 2010) to evaluate recrystallization of calcite and baryte by monitoring the uptake of ^{45}Ca and ^{133}Ba,

respectively, from spiked solutions. While the original co-precipitation models described by McIntire (1963) merely quantify the distribution of a trace element or tracer isotope between aqueous phase and solid by determining specific partition coefficients, the adapted formalisms (denoted homogeneous, HOR, and heterogeneous, HER recrystallization models, respectively) additionally allow to extract kinetic rates of recrystallization.

In a more recent study, Heberling et al. (2018) developed a variant of the HOR model to account for the slowdown of ^{133}Ba removal observed when the same synthetic baryte (Sachtleben baryte) used in the tests of Curti et al. (2010) was pre-equilibrated during several months in a saturated aqueous solution. In this variant, dubbed Continuous HOmogeneous Recrystallization (CHOR) model, it was postulated that recrystallization of the pre-conditioned baryte particles proceeds via repeated dissolution/precipitation cycles, leading to a slower recrystallization kinetics compared to the predictions by the HOR model. Finally, Tits et al. (2024) further extended the CHOR model by coupling it with instantaneous and reversible surface adsorption via distribution coefficient (K_d), to account for the fast adsorption of ^{45}Ca and ^{32}Si radiotracers observed during recrystallization of calcium silicate hydrates (C-S-H) in cement waters.

In contrast to HOR and CHOR, the HER model assumes partial equilibrium during co-precipitation. Only a thin surface layer is in thermodynamic and isotopic equilibrium with the aqueous phase. The newly formed solid grows close to, but at a distinct location from the primary dissolving solid, leading to a zoned tracer isotope distribution (see Fig. 3–5 in Curti, 1997).

D/P-driven recrystallization ("atom exchange" in the original terminology) was also studied on redox-sensitive iron minerals such as goethite, hematite, and magnetite, in aqueous solutions (Gorski and Fantle, 2017; Frierdich et al., 2014a, 2014b, 2015a, 2015b, 2019a, 2019b; Taylor et al., 2019; Joshi et al., 2022)using methods partly similar to those previously described. For instance, Joshi et al. (2017, 2022) spiked nanoparticulate goethite suspensions with ^{55}Fe and monitored its removal from solution in a fully analogous way as in the aforementioned baryte studies. Handler et al. (2009) and Frierdich et al. (2015a) used instead a technique based on stable isotopes of iron, which required a more sophisticated data evaluation. Recently, Joshi et al. (2022) presented a generic model (the "back-reaction" model) to derive recrystallization rates from the Fe-isotope exchange data that has some analogies to the CHOR model.

The main objective of the present paper is threefold. Firstly (Section 2), we provide a rigorous and complete formal treatment of the HOR and CHOR models (henceforth referred together as C(HOR)), including coupling with instantaneous reversible adsorption (K_d approach). Section 3 is then devoted to the review and kinetic modeling of experimental recrystallization data obtained in the past two decades on a variety of minerals (baryte, calcite, goethite, calcium-silicate hydrates and UO$_2$). Published data on goethite recrystallization are discussed in detail after re-modeling with the C(HOR) approach, and the results compared with those of the models applied in the original publications. Technical details and additional case studies are given in S3. Finally, Section 4 provides a discussion of the driving forces governing D/P-driven recrystallization, a comparison of the C(HOR)-K_d approach with the "back-reaction" model of Joshi et al. (2022), a correlation between solubility and recrystallization kinetics, and a graphical synthesis of the obtained model results combined for several minerals.

Overall, this contribution can be regarded as an update of a former review (Gorski and Fantle, 2017) as it includes a discussion of a considerable number of papers published later, or not considered in the former review.

2. Mathematical model formalism

2.1. Introductory remarks

In this Section, the mathematical formalism underlying the C(HOR) model is presented in a more generalized form than in earlier publications, including the coupling to instantaneous linear sorption. Moreover, variants of the HOR and CHOR models that apply specifically to recrystallization of layered-structure minerals, such as clay minerals and calcium silicate hydrates, are presented in S2, which also includes mathematical demonstrations and the full details of all four model variants.

The C(HOR) models are inspired to the pseudomorphic replacement model (PRM) (Putnis and Putnis, 2007; Putnis, 2009; Putnis, 2015) which describes in-situ replacement of a primary dissolving solid by a secondary, thermodynamically more stable solid of different chemical composition or crystal structure. The C(HOR) approach is analogous to PRM in that it postulates in-situ replacement of the initial volume "from outside inward" by a new solid phase via dissolution and re-precipitation, however the re-precipitating solid in essentially iso-chemical and isostructural with the primary solid, i.e. the same solid transforms in itself under stable chemical conditions close to saturation. The latter is a stringent requirement that differentiates recrystallization from the transformation of the primary solid in a completely different stoichiometry or another polymorph implied by the PRM model.

2.2. HOR model formalism

Both CHOR and HOR postulate a closed system in which the primary solid consists of equally sized cubic particles (monodispersed grain size distribution) with edge length a_0 [m] immersed in a fixed volume of aqueous solution. Each cubic particle is made up of concentric "monolayers" of equal thickness d [m], defined via crystallographic criteria (Fig. 1). A monolayer is the smallest unit removed by dissolution and reconstructed by re-precipitation. As the first monolayer of the primary pure mineral is dissolved, it re-precipitates at the same place. Another implicit assumption of the model is that the re-precipitation rate must be at least as fast as the dissolution rate, otherwise the postulated assumptions of volume conservation and constant solubility would break

down. Furthermore, it is assumed that the recrystallized solid is permeable to the aqueous solution, so that it can reach progressively more internal parts of each single cubic particle. For a recrystallization experiment conducted with a solid of specific weight ρ [kg m^{-3}] at a solid/liquid ratio $(S/L)_0$ [kg m^{-3}] in a volume V [m^3] of aqueous solution, the total number of particles N is:

$$N = \frac{(S/L)_0 V}{\rho \, a_0^3} \tag{1}$$

The recrystallization of k mineral layers thus produces the following amount $n(k)$ [mol] of recrystallized secondary solid:

$$n(k) = \frac{(S/L)_0 V}{W \, a_0^3} \left[a_0^3 - (a_0 - 2kd)^3 \right] \tag{2}$$

where W [kg mol^{-1}] is the molar weight of the recrystallizing solid. The term in square brackets arises from the assumed geometry; it describes the increasing volume of recrystallized solid as the aqueous solution front proceeds from the outside towards the center of the cubic particles. Further, it is assumed that recrystallization proceeds at a constant surface-normalized rate R_e [mol m^{-2} s^{-1}] defined as:

$$R_e \equiv \frac{\Delta n_{(k=1)}}{S_0 \Delta t} \tag{3}$$

where S_0 [m^2] $\equiv S_{(k=1)}$ is the initial exposed surface area of the solid (assumed to be equal to the integrated geometric surface area of the cubic particles), $\Delta n_{(k=1)}$ is the total molar amount of primary solid in the first (most external) monolayer integrated over all particles, and Δt [s] is the corresponding recrystallization time. The quantity $\Delta n_{(k=1)}$ can be expressed as follows:

$$\Delta n_{(k=1)} = \frac{d \, S_0 \, \rho}{W} \tag{4}$$

Substituting Eq. (4) into Eq. (3) and rearranging yields then the monolayer recrystallization time:

$$\Delta t = \frac{d \, \rho}{W \, R_e} \tag{5}$$

Note that Δt is a constant applying to *all* monolayers, not just the most external one. This is simply a consequence of postulating a constant
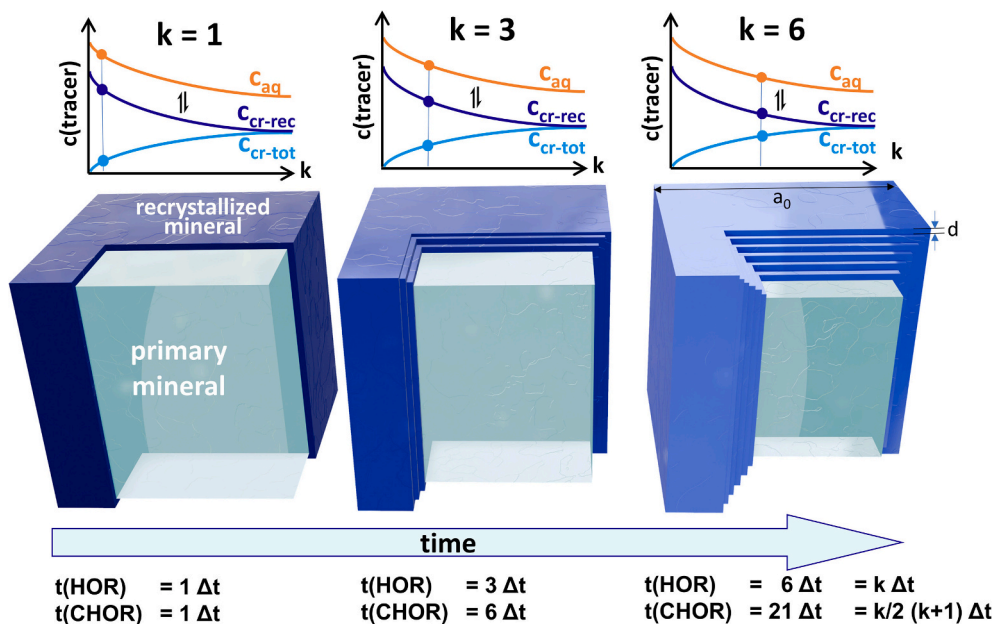
Fig. 1. 3D-sketch showing the layer wise evolution of a cubic solid particle and the different time calculations used in the HOR and CHOR models (k = monolayer number). The graphs on top show schematically the evolution of tracer concentrations in aqueous phase (C_{aq}), recrystallized solid (C_{cr-rec}) and total solid (C_{cr-tot}).

surface-normalized recrystallization rate. Indeed when Eq. (3) and Eq. (4) are applied for a generic index value k (using S_k instead of S_0) and the previous substitution is carried out, it can be easily seen that S_k cancels out, resulting in the same expression given by Eq. (5). Therefore, the cumulative time required to recrystallize k monolayers predicted by the HOR approach, is simply:

$$t_k = k\Delta t = \frac{k\,d\,\rho}{W\,R_e} \tag{6}$$

To express Eq. (2) as an explicit function of time rather than of monolayer number, we substitute into the latter equation $k\,d = W\,R_e\,t/\rho$ from Eq. (6) and obtain:

$$n(t) = K\left[a_0^3 - \left(a_0 - \frac{2\,W\,R_e\,t}{\rho}\right)^3\right] \tag{7}$$

where $K \equiv \frac{(S/L)_0 V}{W\,a_0^3}$.

Eq. (7) predicts the time-dependent amount of primary solid recrystallized as a function of solid's properties (ρ, W, a_0), experimental parameters (($S/L)_0$, V) and the recrystallization rate, R_e, which is the main adjustable parameter used to fit the data. Note that because R_e is correlated to the somewhat arbitrary value of the monolayer thickness, d, (via Δt, see Eq. (5)), the fitted value of R_e is in general affected by considerable uncertainty. This issue is discussed in Section 4.2.

Next, the net amount of primary solid recrystallized, $n(t)$, has to be related to the experimental quantity used to monitor the process. In most cases, it is the gradually decreasing activity of a radiotracer in a spiked solution saturated with the solid of interest (Curti et al., 2005; Curti et al., 2010; Heberling et al., 2018; Joshi et al., 2017; Joshi et al., 2022; Tits et al., 2024). The implicit assumption is that the disappeared radiotracer is *fully* incorporated in the recrystallized fraction of the solid, i.e., that there are no competitive sinks for the radiotracer such as adsorption sites on the solid itself, vessel walls or escape to a gas phase in the case of volatile tracers. Under this premise, the decrease in radiotracer activity (or concentration) is described by following equation:

$$\frac{A_L(t)}{A_{tot}(t)} = \frac{C_s V}{r\,n(t) + C_s V} \tag{8}$$

$A_{tot}(t)$ and $A_L(t)$ are the total (decay corrected) radiotracer activity in the system and the measured activity in the aqueous phase at time t after the start of the experiment, respectively. C_s is the saturation concentration of the radiotracer's carrier element (e.g. Ba for ^{133}Ba in baryte, Ca for ^{45}Ca in calcite) which must be constant during the experiment, a condition that should always be verified experimentally. Finally, r is the stoichiometric coefficient of the tracer's carrier element in the recrystallizing mineral's formula (e.g. $r = 1$ for ^{45}Ca tracer uptake by calcite, using $CaCO_3$ as formula).

2.3. CHOR model formalism

Both HOR and CHOR models postulate monolayer-by-monolayer homogeneous recrystallization from outside towards the internal part of the primary cubic solid particles, as shown in Fig. 1. At any time, the recrystallized fraction is assumed to be in a local, temporary equilibrium with the aqueous solution, which is continuously adjusted during the advancement of the recrystallization front. However, while in the HOR model the time Δt, needed for recrystallization of each newly added more internal monolayer, is constant (see Eq. (5)), in the CHOR model Δt increases proportionally to the number of previously recrystallized monolayers, as a consequence of the repeated dissolution-precipitation cycles. This leads to progressively slower *macroscopic* (bulk) recrystallization rates (R_b) compared to the HOR model, even if the *effective* (intrinsic) recrystallization rate, R_e, remains constant and equal in the two models. The iterative monolayer dissolution/precipitation cycles assumed in CHOR bear some analogy to the concept of "back-reaction"

in the model of Joshi et al. (2022), see Section 4.2.

Note that Eq. (2), which describes the net amount of primary solid recrystallized when the aqueous reaction front has penetrated k monolayers, applies both to HOR and CHOR models. The two mechanisms imply however different values of the recrystallization time, t, for the same net amount of recrystallized solid. While in the HOR model the time required to recrystallize k monolayers is simply the time constant Δt multiplied by k (Eq. (6)), for the CHOR model an additional term t_{k-1} is added to account for the repeated recrystallization of monolayers:

$$t_k = \Delta t\,(1 + 2 + 3 + ...k) = t_{k-1} + k\Delta t \tag{9}$$

It is evident from the comparison of Eq. (6) and Eq. (9) that recrystallization of k monolayers through the CHOR mechanism requires more time than through the HOR mechanism. With CHOR, the macroscopic recrystallization rate will progressively slow down as more and more internal monolayers are reached by the reacting front. The recursion term t_{k-1} in Eq. (9) can be replaced using the analytical solution of the arithmetic series $(1 + 2 + 3 + ... k)$ yielding (see S2 for demonstration):

$$t_k = \frac{k}{2}(k+1)\Delta t \tag{10}$$

An explicit solution for $n(t)$ analogous to Eq. (7), in which the recursion counter k is eliminated and replaced by the reaction time, t, can be obtained also for the CHOR model (see demonstration in S2):

$$n(t) = K\left\{a_0^3 - \left[a_0 + d\left(1 - \frac{\sqrt{\Delta t^2 + 8\,t\Delta t}}{\Delta t}\right)\right]^3\right\} \tag{11}$$

The decrease in radiotracer activity can then be predicted, as for the HOR model, using the same Eq. (8), however substituting Eq. (11) instead of Eq. (7) for $n(t)$.

2.4. Definition of recrystallization rates

The "effective" recrystallization rate (R_e, mol m^{-2} s^{-1}) implicit in Δt, see Eq. (5), and the "bulk" recrystallization rate (R_b, mol m^{-2} s^{-1}) must be clearly distinguished. R_e represents the rate at which the mineral dissolves and re-precipitates at the scale of a single monolayer and is constant and equal in both HOR and CHOR models. This is the main parameter to be adjusted in order to fit experimental data. In contrast, R_b is the macroscopically observed mean rate, i.e. the cumulative *net* amount of mineral recrystallized at any time t during the recrystallization process divided by the elapsed recrystallization time and initial exposed surface area, which is computed for both HOR and CHOR models by dividing the derived explicit $n(t)$ expressions (Eq. (7) and Eq. (11), respectively) by $S_0 = \sigma_0\,(S/L)_0\,V$ and t:

$$\text{HOR}: R_b(t) = \frac{a_0^3 - \left(a_0 - \frac{2d\,t}{\Delta t}\right)^3}{W\,a_0^3\,\sigma_0\,t} \tag{12}$$

$$\text{CHOR}: R_b(t) = \frac{a_0^3 - \left[a_0 + d\left(1 - \frac{\sqrt{\Delta t^2 + 8\,t\Delta t}}{\Delta t}\right)\right]^3}{W\,a_0^3\,\sigma_0\,t} \tag{13}$$

An additional rate, the "instantaneous" bulk recrystallization rate (R_i, mol m^{-2} s^{-1}), is defined by determining the time derivatives of Eq. (7) and Eq. (11) and dividing them by S_0:

$$\text{HOR}: R_i(t) = \frac{6\,d\left(a_0 - \frac{2\,d\,t}{\Delta t}\right)^2}{W\,a_0^3\sigma_0\Delta t} \tag{14}$$

$$\text{CHOR}: R_i(t) = \frac{12\, d \left[d \left(1 - \frac{\sqrt{8t\Delta t + \Delta t^2}}{\Delta t} \right) + a_0 \right]^2}{W\, a_0^3\, \sigma_0 \sqrt{8t\Delta t + \Delta t^2}} \tag{15}$$

Fig. 2 shows exemplary HOR model results calculated for $R_e = 0.7$ µmol m^{-2} d^{-1} and a suspension of 360 mg C-S-H recrystallizing in 40 ml of 2.2 mM Ca solution.

Fig. 2a shows the calculated HOR model curve of the amount recrystallized, $n(t)$, along with three straight lines with slopes corresponding to time derivatives defining R_b and R_i at 100 days and R_e. Note that the straight line for R_e can only be drawn as tangent to $n(t)$ at $t = 0$, the only time at which the three rates converge to identical values, however it applies to all times, as it is a model constant. Fig. 2b shows the corresponding rate functions derived from the slopes of the $n(t)$ curves and defined mathematically by Eq. (14) and Eq. (15). The choice of $t = 100$ days in Fig. 2a is arbitrary and serves merely to illustrative purposes. R_e, R_b, R_i are rates normalized to the initial surface area, but can be easily transformed to non-normalized rates [mol s^{-1}], as used e.g. in Joshi et al. (2022), via multiplication by the factor $S_0 = 6\, a_0^2\, N$.

2.5. Coupling with adsorption

Recrystallization tests on C-S-H phases with ^{32}Si and ^{45}Ca tracers (Tits et al., 2024) showed an abrupt decrease by up to 50 % of the aqueous radiotracer activity in less than one day upon contact of the solid with the spiked solution. This decrease is too fast to be explained by D/P-driven recrystallization alone and is a clear indication for rapid isotopic exchange at the mineral surface. In order to fit the data, it was necessary to extend the CHOR model by including a surface adsorption model. This was done by linking a simple model for linear instantaneous adsorption (K_d-approach) to Eq. (8), resulting in the following extended general equation (see S2 for demonstration):

$$\frac{A_L}{A_{tot}} = \frac{C_s V}{r\, n(t) + K_d\, C_s (S/L)_0 V + C_s V} \tag{16}$$

where K_d [m^3/kg] is a constant distribution coefficient describing the instantaneous reversible isotopic exchange of the tracer in aqueous solution with its stable isotopes at the mineral surface, defined as a fixed ratio of surface adsorbed to dissolved concentrations. Although the adsorption requires a few hours and is thus not strictly instantaneous, the K_d-approach is a good approximation, as the time scale of the D/P-driven recrystallization, which requires far more extensive bond breaking and reconstruction, is orders of magnitude slower. In cases where adsorption is negligible, the K_d value can be set to zero and Eq. (16) simplifies to Eq. (8).

Because Eq. (16) just links the experimentally measured radiotracer activity with a generic $n(t)$ function describing the net macroscopic amount of solid recrystallized, it is valid for both HOR and CHOR models. Moreover, it is important to realize that in both models $n(t)$ and the rate functions are related to recrystallization only. Therefore, any failure to consider tracer adsorption on the solid or reactor equipment, or any loss to other sinks, would result in overestimation of the amounts recrystallized and rates of recrystallization. If fast adsorption and recrystallization are distinguished neatly by careful measurements, the model curves illustrated in Fig. 2 are not affected by adsorption, i.e. they will be identical whether or not fast surface adsorption occurs.

In sorption studies on the immobilization of hazardous contaminants, it is common practice to present the results of experiments in which a dissolved species is scavenged from the aqueous solution via generic aqueous/solid interactions in the form of a global distribution coefficient, R_d [m^3/kg] (e.g., Marques Fernandes et al., 2008). This quantity is a global distribution ratio incorporating all tracer-scavenging processes contributing to the decrease in dissolved tracer concentration. For the combined effect of recrystallization and instantaneous adsorption, R_d is defined as:

$$R_d = \frac{n(t)}{C_s\, (S/L)_0 V} + K_d \tag{17}$$

Fig. 3 shows exemplarily the effect of specific K_d-values on tracer activity in solution and R_d for the hypothetical case illustrated in Fig. 2.

3. Application of C(HOR)-K_d model to case studies

3.1. Baryte

In spite of its low solubility product (log10 $Ks^0 = -9.96 \pm 0.07$ at 25 °C, Brown et al., 2019) baryte has long proved to undergo fast dynamic recrystallization, as shown in an early study by Doerner and Hoskins (1925). Curti et al. (2010) and Heberling et al. (2018) carried out similar recrystallization experiments on *pure* commercial baryte (Sachtleben baryte, shortly SL) under milder, geochemically more realistic conditions (room temperature, near-neutral pH). Moreover, the use of ^{133}Ba as radiotracer allowed determining recrystallization rates.

Selected results from the two latter studies are combined in Fig. 4, showing the ratio of ^{133}Ba activity in solution to total (decay corrected) activity in the system as a function of the *effective total* contact time of the solid with the aqueous solution (denoted "recrystallization time"). Data and model results are shown in both linear (Fig. 4a) and semi-log scale (Fig. 4b). The integrated modeling of the two experiments shows that while the data from exp. 9, obtained with untreated baryte, follows the HOR formalism (the CHOR and HET models fail, see Fig. 4b) the data from exp. A, obtained after 284 days pre-equilibration, follow the CHOR model formalism.

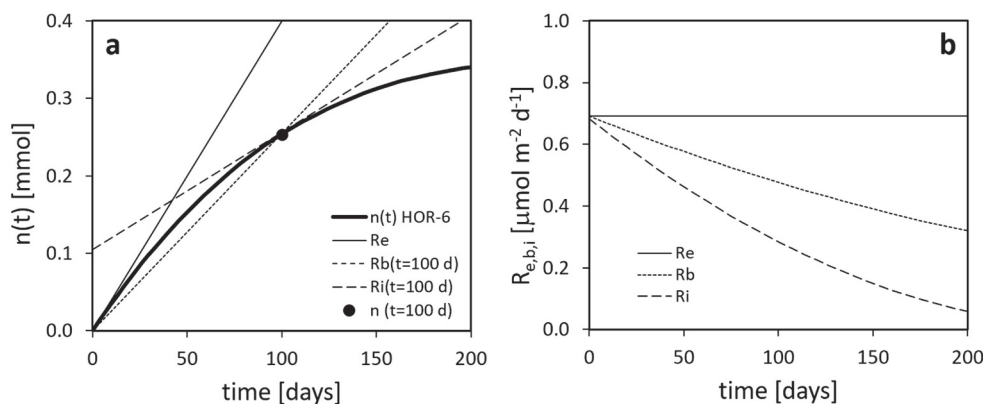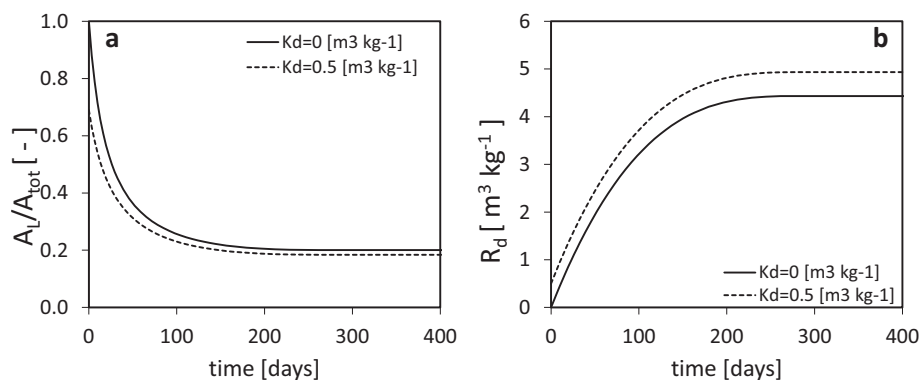In order to understand the reasons for this difference in

Fig. 2. (a) Graphical definition of effective (R_e), bulk (R_b) and instantaneous (R_i) recrystallization rates, based on time derivatives (slopes) of the $n(t)$ function; (b) corresponding rate functions.

Fig. 3. Effect of instantaneous reversible adsorption during recrystallization of a solid on the radiotracer activity in solution (a) and on the global distribution coefficient R_d (Eq. (17)) for the same parameter set used to generate Fig. 2.
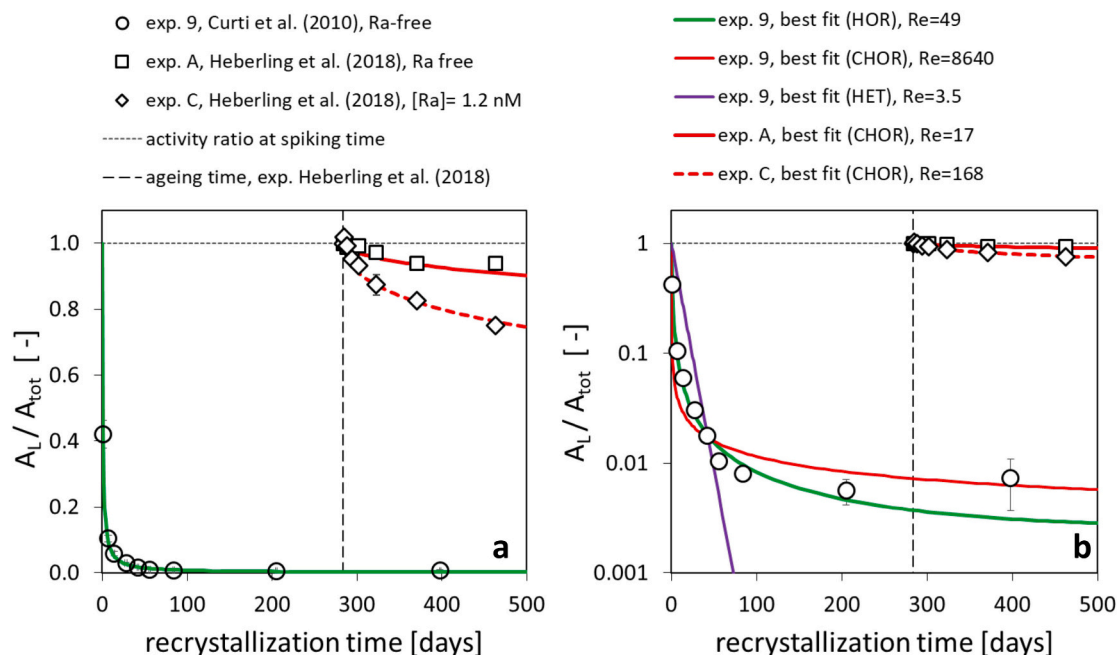
Fig. 4. Selected data on SL baryte recrystallization shown as ratio of ^{133}Ba activity in solution (A_L, Bq) to total system activity (A_{tot}, Bq) as a function of the total interaction time of the solid with aqueous solution. The HOR model curve of exp. 9 is identical to that presented in Curti et al. (2010).

recrystallization regime Heberling et al. (2018) measured the XRD patterns of the untreated SL baryte, as well as after 284 days and 4 years pre-equilibration in the same solution used in the recrystallization tests. The pristine, non-aged SL baryte showed broad low-intensity reflections indicative of poor crystallinity. Upon prolonged contact with the aqueous solution due to pre-equilibration, the XRD reflections narrowed and became more intense, indicating a progressive increase in the size of coherent crystal domains. The largely different macroscopic rates (R_b) extracted from the tests with untreated and pre-equilibrated baryte thus point to a key role of crystallinity in determining the net pace of the recrystallization process, possibly related to a decreased accessibility of the aqueous solution (e.g. along crystallite boundaries) in the pre-aged baryte.

Experiments in 0.5 g l^{-1} suspensions, conducted over a time span of up to 883 days in Ra-bearing solutions (Brandt et al., 2015), revealed for SL and another commercial baryte (Aldrich) a complex kinetics characterized by three distinct stages: (1) rapid decrease of aqueous Ra concentrations during the first 100–200 days (from $\approx$ 2–4 $\times$ 10^{-6} M to $\approx$ 1 $\times$ 10^{-6} M) at $R_b \approx$ 0.4–3 µmol m^{-2} d^{-1}; (2) an abrupt fall of Ra concentration to 2–4 $\times$ 10^{-8} M in the subsequent 100 days; and (3) a weak but steady Ra concentration increase (up to 7–8 $\times$ 10^{-8} M) during the

remaining 580–680 days. Whereas stage (1) may correspond to the HOR-type recrystallization process observed by Curti et al. (2010), the abrupt decrease in Ra concentration observed in stage (2) with inferred macroscopic recrystallization rates in the order of 400 µmol m^{-2} d^{-1} cannot be interpreted with the CHOR model as in the case of the experiment of Heberling et al. (2018) with pre-equilibrated baryte, as the kinetics accelerates instead of slowing down. Brandt et al. (2015) explain this unexpected observation with sudden surface nucleation of Ra-baryte from solution (which is saturated with respect to pure baryte, but supersaturated with respect to Ba$_{1-x}$Ra$_x$SO$_4$). The TEM and SEM data of Weber et al. (2017) suggest that nucleation of Ra-baryte in stage (2) started on the internal surfaces of macropores present in the pristine SL baryte, possibly driven by the low interfacial tension between the Ra-poor substrate and the newly formed Ra-rich baryte (heterogeneous nucleation). The late gradual, weak increase in Ra-concentration during stage (3) was then explained by slow recrystallization of the metastable Ra-baryte formed during stage (2) into thermodynamically stable solid solution, a process which likely follows the slower CHOR pathway. Unfortunately, this anticipation cannot be verified via C(HOR) modeling because the experiments were carried out without ^{133}Ba tracer.

The question arises why the complex kinetic pattern observed in the

experiments of Brandt et al. (2015) was not observed neither in the Ra-baryte experiments of Curti et al. (2010) nor in those of Heberling et al. (2018), in spite of the use of identical products (SL baryte), similar aqueous chemistry and comparable experimental conditions. The main difference between the two sets of experiments consists in the largely different concentrations of Ra used. While Curti et al. (2010) and Heberling et al. (2018) carried out their tests in solutions containing very low (nanomolar) radium concentrations, Brandt et al. (2015) used Ra concentrations up to three orders of magnitude higher. Higher supersaturations with respect to the Ra-baryte solid solution were attained compared to the experiments of Curti et al. (2010). This could have favored heterogeneous nucleation of the stage (2) Ra-rich phase on the stage (1) Ra-poor baryte substrate.

This interpretation was indirectly confirmed by Weber et al. (2016, 2017), who provided detailed insight on the evolution of particle features during D/P-driven recrystallization of baryte under the same conditions applied in the experiments of Brandt et al. (2015) and Heberling et al. (2018). After pre-equilibration during 10 weeks in Ra-free pure water or 0.2 M NaCl solution, images obtained by scanning transmission electron microscopy (STEM) coupled with a high-angle annular dark-field (HAADF) detector revealed the SL baryte particles to consist of aggregated euhedral single crystals. Within the crystals, three different pore classes were identified: (a) micrometer-sized macropores; (b) small nanopores (<10) nm and (c) larger nanopores (10–70 nm) aligned in rows parallel to the external crystal faces (Weber et al., 2016). The images clearly showed open connections between macropores and external surfaces of the crystals, presumably allowing the rapid access of aqueous solution to the interior of the particles, as well as a pre-existing pervasive nanoporosity. After prolonged interaction with the aqueous solution, the internal porosity structure of the pure (Ra-free) SL baryte apparently did not undergo significant changes (Weber et al., 2017). In contrast, when the experiment was repeated in the presence of high (micromolar) Ra concentrations, after about 100 days interaction with the aqueous phase both particle morphology and internal porosity structure changed quickly and dramatically, and the initially pure SL baryte transformed into radiobaryte solid solution.

3.2. Calcium Silicate Hydrates (C-S-H)

Fig. 5 shows the normalized ^{45}Ca radiotracer activity measured in the spiked solution (symbols) for selected experiments carried out by Tits et al. (2024) with calcium silicate hydrates (C-S-H) along with corresponding best fits obtained using the CHOR model coupled with linear reversible adsorption (Section 2.5). The data refer to three separate tests carried out at different solid to liquid ratios ($S/L \approx 1$, 4 and 10

g l^{-1}), using C-S-H phases of almost identical composition, i.e. at Ca:Si ratio (C/S) ≈ 1.0. Fig. 5a shows a two stage uptake kinetics, consisting of quasi-instantaneous sorption (35 % - 75 % of the initial ^{45}Ca activity removed within 1 day, the percentage increasing with S/L-ratio) followed by much slower uptake during up to 400 days, ascribed entirely to D/P-driven recrystallization, as wall sorption effects were proved to be negligible. The same data and model results are also presented as global sorption coefficient (R_d, m^3 kg^{-1}) as a function of recrystallization time (Fig. 5b). The R_d-value at the origin ($t = 0$) coincides with the postulated K_d-value, while the subsequent increase represents the contribution due to recrystallization. Both plots show that, as expected, the removal of ^{45}Ca activity from solution increases with increasing S/L ratio.

All data could be satisfactorily reproduced using the CHOR model, while application of the HOR model (not shown) failed in all cases. Because the three tests shown in Fig. 5 are essentially replicas of the same experiment, differing only by S/L ratios and spike concentrations, one expects the same effective recrystallization rate to be derived for the three tests. This anticipation was nearly, however not entirely met, as the extrapolated R_e values were within the same order of magnitude (0.06, 0.21 to 0.45 µmol m^{-2} day^{-1}) but differed significantly. Analogous experiments carried out with ^{32}Si tracer (not shown) yielded similar effective recrystallization rates ($R_e = 0.08–0.26$ µmol m^{-2} day^{-1} up to 50 days recrystallization time) and even higher adsorption coefficients. ($K_d = 32$ m^3/kg had to be assumed to reproduce the ^{32}Si data).

The contribution of adsorption (probably related to the high specific surface area of the nanometer-sized C-S-H particles) is evidenced in Fig. 5a by the low A_L/A_{tot} values after 1 day and must be necessarily included in the CHOR model to obtain successful fits.

3.3. Goethite

Joshi et al. (2017) and Frierdich et al. (2015a) studied the Fe(II)-catalyzed recrystallization of synthetic goethite suspensions (FeOOH) in Fe(II)-bearing solutions under controlled anoxic conditions. The recrystallization process ("atom exchange" in the original terminology of these authors) was monitored using two distinct techniques: (a) the usual radiotracer method (^{55}Fe-spike, half-life 2.7 years) in the experiments of Joshi et al. (2017), and (b) a method based on the exchange of stable isotopes of iron and oxygen (^{57}Fe and ^{17}O enriched aqueous solutions), in the tests of Frierdich et al. (2015a). While in the former case the evaluation of the isotopic data is fully analogous to that applied to ^{133}Ba-spiked baryte, the stable isotope data required a more sophisticated evaluation technique, due to natural abundances of ^{57}Fe and ^{17}O present in the starting solutions. Dedicated models were developed in both original studies that can reproduce the experimental data
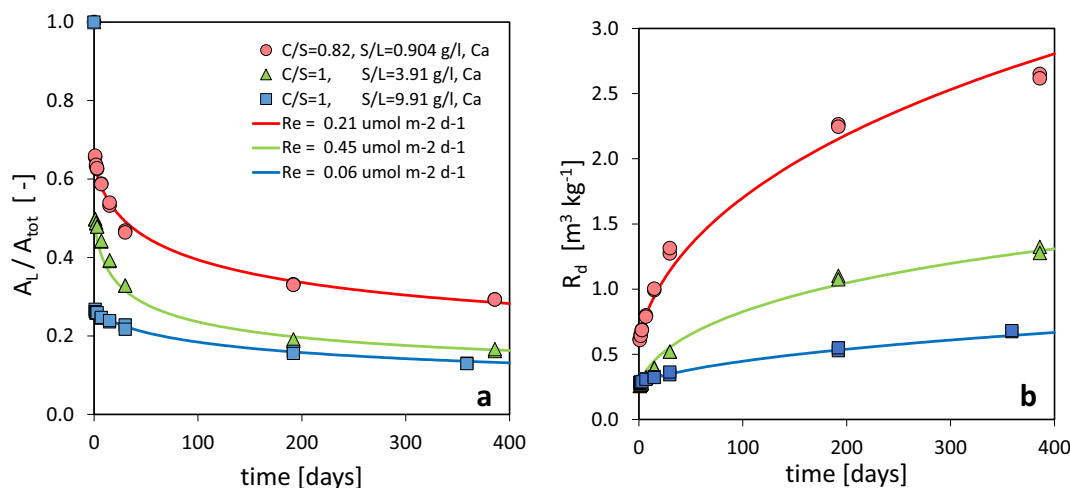

Fig. 5. Selected data from Tits et al. (2024) and corresponding model fits for exchange of ^{45}Ca with C-S-H phases obtained with the CHOR model coupled with linear instantaneous reversible adsorption (K_d approach). Analogous fits with HOR model failed (not shown).

satisfactorily. Here, we show that both datasets can be re-modeled successfully using the C(HOR) approach. An in-depth discussion and comparison with the original model results is deferred to Section 4.

Two separate experiments were carried out by Joshi et al. (2017) using nanoparticulate goethite (6–60 nm grain size, specific surface area 87.8 ± 0.4 m^2/g). In the first experiment, ^{55}Fe spike was added after one day pre-equilibration time, while in the second otherwise identical test the ^{55}Fe spike was added after 30 days of pre-equilibration. The combined results of the two experiments are represented as a single consecutive "double-spike" experiment (as done in Fig. 2 of Joshi et al., 2022) in Fig. 6 with the corresponding C(HOR) model best fits.

Upon first spike addition after 1 day pre-equilibration, ($t = 1$ day), the ^{55}Fe activity in solution follows a fast decrease that can be fitted using the HOR model with $R_e = 4.3$ µmol m^{-2} d^{-1}. In contrast, the data for the test carried out after 30 days pre-equilibration time ($t = 30$ days) requires the CHOR model with a two orders of magnitude lower intrinsic recrystallization rate ($R_e = 0.034$ µmol m^{-2} d^{-1}). This pattern is analogous to that observed in the combined evaluation of the baryte experiments of Curti et al. (2010) and Heberling et al. (2018), see Fig. 4. For both goethite tests, we set $K_d = 0.3$ m^3/kg to capture the initial fast decrease in activity, and almost identical constant Fe concentrations were assumed ($C_s = 0.66$ and 0.56 mM for the "first" and "second" spiking, respectively), based on the available data (Table S5 in Joshi et al., 2017). The data point at 60 days (open square in Fig. 6) was excluded from the fitting as it corresponds to an unexplained decrease in Fe concentration (by more than 50 % between 45 and 60 days), which breaks down the constant Fe saturation condition required by the C(HOR) models.

Frierdich et al. (2015a) investigated goethite recrystallization using a spike enriched in natural stable isotopes of iron (^{57}Fe) and oxygen (^{17}O). In Fig. 7 we show that the bulk amounts of exchanged Fe determined by Frierdich et al. (2015a) can be satisfactorily reproduced using the C(HOR) models. Two sets of recrystallization data (four datasets in total) extracted from experiments conducted at 22 °C and 50 °C were considered. The original data, expressed as percentage of total Fe atoms in goethite exchanged, were first converted to $n(t)$, the mole amount of goethite recrystallized, and then fitted using experimental parameters quoted in (or derived from) Frierdich et al. (2015a) ($V = 10$ ml, $S/L = 2.02$ g l^{-1}, $\sigma_0 = 119$ m^2/g, $C_s = $ [Fe] $\approx 6 \times 10^{-4}$ M). The same values of specific weight (4.3 g cm^{-3}) and monolayer thickness ($d = 4$ Å) used for the C(HOR)-K_d modeling of the data of Joshi et al. (2017) were selected as fixed parameters, leaving R_e and K_d as fit parameters to be adjusted.

Model optimization showed failure of the HOR model to reproduce the four datasets, while application of the CHOR model led to satisfactory fits assuming for the data at 22 °C and 50 °C, $R_e = 3.46$ and 21.6

Fig. 7. Transformed stable isotope data from Frierdich et al. (2015a) expressed as moles of goethite recrystallized, $n(t)$, as a function of recrystallization time, along with C(HOR) best fits. Squares and circles refer to experiments obtained at 50 °C and 22 °C, respectively, in two different tap waters (denoted FB and H) using nano-goethite (n-Gth, 119 m^2 g^{-1}). Numbers in parentheses indicate best fit R_e values in µmol m^{-2} d^{-1}.

µmol m^{-2} day^{-1}, respectively. The R_e-value for the 22 °C data compares well with the short-term R_e-value determined via HOR for Joshi et al. (2017) short-term data (4.3 µmol m^{-2} d^{-1} for $t = 1$–30 days).

Although the CHOR modeling yields fits (Fig. 6) fully equivalent to those obtained by Joshi et al. (2022) with the "back reaction" model for the same data (Frierdich et al., 2015a) the predicted amounts of recrystallized goethite are different (67 % vs. 18 % during the first 30 days, 44 % vs. 1.8 % for the subsequent 30 days, see Fig. 13 in the present paper and Table 1 in Joshi et al., 2022). We do not have an explanation for this discrepancy, however we note that the amounts predicted with the CHOR model are fully consistent with the percentages of goethite recrystallized determined by Frierdich et al. (2015a), while the model of Joshi et al. (2022) strongly underpredict them.

3.4. Uranium(IV) oxide

Olilla (2006, 2008) carried out static interaction tests in NaCl solutions (up to 0.1 M) with 1.1–4 mm sized fragments of non-irradiated UO$_2$ pellets in aqueous solutions enriched in ^{235}U, at aqueous U concentrations close to the expected saturation level. The $n(t)$ data (Fig. 8) align along a quasi-linear trend fairly well reproduced by both HOR and CHOR, defining a restricted range of effective recrystallization rates with either model ($R_e = 0.8$–1.3×10^{-13} mol m^{-2} s^{-1} and 6.9–11.2 nmol m^{-2} day^{-1}, respectively). These are by far the lowest rates among those discussed in this paper, implying an extremely long monolayer dissolution time ($\Delta t = 1796$ days). Because the experimental data extended over 250 days only, the
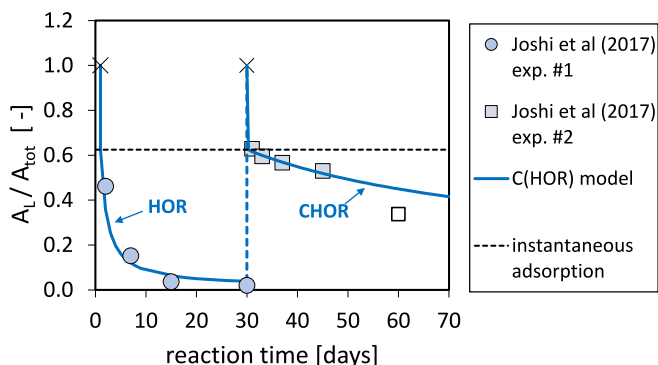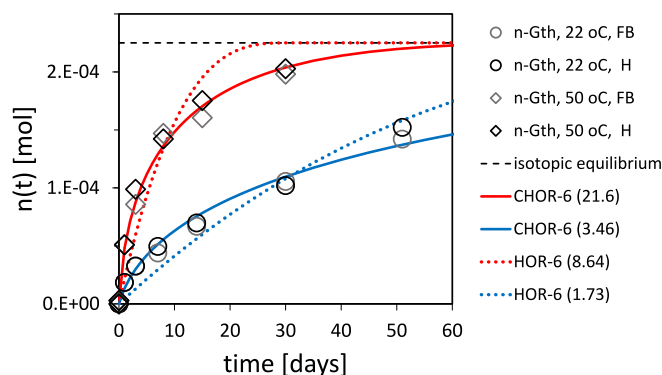

Fig. 6. ^{55}Fe activity data from Joshi et al. (2017) (symbols) with best fits (curves) obtained from the HOR and CHOR models. Crosses show A_L/A_{tot} values at spiking time (unity by definition), while the horizontal broken line indicates the reduction ascribed to instantaneous adsorption, assuming $K_d = 0.3$ m^3/kg for both tests. The open square is a data point excluded from the fit due to an abrupt Fe concentration fall.

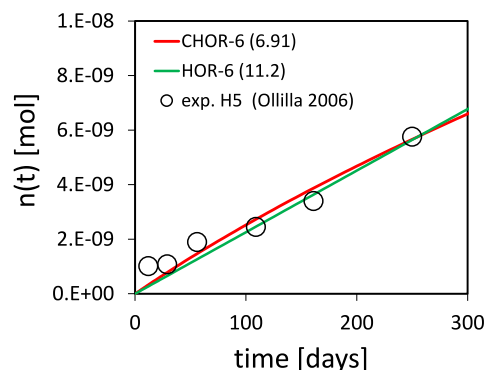**Fig. 8.** Selected UO$_2$ recrystallization data from Olilla (2006), expressed as moles of solid recrystallized as a function of interaction time, compared to best fits for CHOR and HOR models. Number in parentheses indicate the derived R_e values in nmol m^{-2} day^{-1}.

implication of the C(HOR) model prediction is that [235]U isotope exchange between solid and solution was limited to the first most external monolayer. The data thus essentially record a slow surface-limited isotope exchange process that cannot be classified as fast reversible surface adsorption, but rather as incipient recrystallization.

3.5. Calcite

Heberling et al. (2016) carried out isotope exchange experiments with synthetic and natural calcite powders differing in terms of particle size, crystal habitus and "surface roughness", using solutions spiked with [45]Ca radiotracer. "Surface roughness" is a generic term denoting the departure of mineral surfaces from ideal, perfectly flat crystal surfaces and increases with the density of steps and other types of crystal defects following e.g. mechanical breaking of the solid. Selected data from that study are shown in Fig. 9 along with the corresponding C(HOR) model fits. The modeling results indicate that datasets showing fast [45]Ca-uptake ("fine grained" and prismatic calcite) follow the HOR formalism, while those showing slow [45]Ca-uptake (scalenohedral and rhombohedral calcite) can only be fitted with the CHOR model. Overall, the extracted intrinsic recrystallization, R_e, differed by almost three orders of magnitude, from 0.04 µmol m^{-2} d^{-1} for rhombohedral to 17.28 µmol m^{-2} d^{-1} for "fine grained" calcite, with intermediate values for prismatic and scalenohedral calcite (1.73 and 2.59 µmol m^{-2} d^{-1}, respectively) however following different formalisms (HOR and CHOR, respectively). SEM images suggest that the different recrystallization models required to fit the data of prismatic and scalenohedral calcite probably reflect distinct recrystallization pathways: while prismatic calcite showed indications for major particle reconstruction towards rhombohedral habitus, the scalenohedral calcite particles only showed signs of surface smoothing, without change in habitus.

Rhombohedral particles were by far the least reactive (R_e = 0.043 µmol m^{-2} d^{-1}, see Fig. 9), probably because of the inherent stability of the rhombohedric habitus coupled with a low degree of "surface roughness". Heberling et al. (2016) argued that the slow [45]Ca uptake kinetics of rhombohedral calcite probably reflects residual dynamic exchange equilibrium between kink sites and fluid at saturation conditions. They supported this conclusion based on the very small amount recrystallized after more than 500 days (corresponding to a single monolayer), and on the activation energy obtained from an Arrhenius plot when this R_e-value is plotted along with the high-temperature rate data of Beck et al. (1992). In contrast, the fast R_e values inferred for "fine grained" calcite can be assigned to the annealing of the high initial "surface roughness" combined with a change in crystal morphology
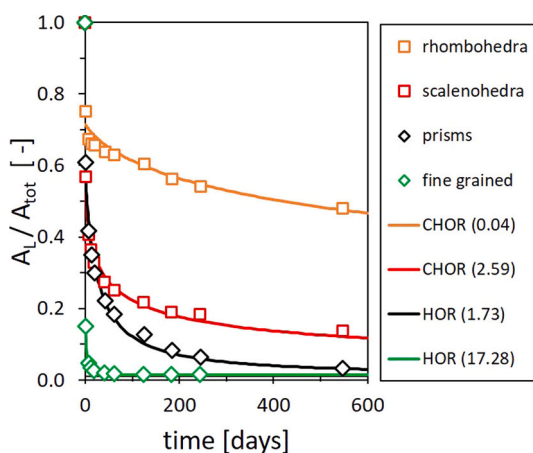
(from rough, irregular, rounded particles towards euhedral, smooth, rhombohedra).

Heberling et al. (2016) also measured [45]Ca exchange between aqueous solution and freshly ground Iceland spar calcite (Fig. 10). After grinding, the particles exhibited extremely rough surfaces, leading upon immersion in the spiked aqueous solution to even faster short-term recrystallization than for fine grained commercial calcite ("fine grained" curve in Fig. 9) and even to a transient increase in solubility (Fig. 10). More than 90 % of the initial activity was removed from solution after 1 day, which was explained by the high density of surface defects and steps implying a high "surface roughness" contribution to the free energy. After 20 days, the [45]Ca activity in solution reached a minimum (98 % of initial activity removed) corresponding almost exactly to the calculated [45]Ca activity ratio at attainment of isotopic equilibrium for this specific system (A_L/A_{tot} = 0.0143 and t_{eq} = 22.3 days). Up to this time, the data can be modeled perfectly using the HOR model with K_d = 2.3 m^3/kg. After about 20 days, the [45]Ca activity in solution rises slightly again, to reach an almost constant A_L/A_{tot} value of about 0.02. Further model calculations show that this increase can be matched almost entirely by assuming reduction of the exposed surface via particle coarsening (confirmed by SEM images). The reduced surface area causes partial desorption of the previously adsorbed [45]Ca, which can be expressed in the C(HOR) model through a decrease in the K_d value from 2.3 to 0.1 m^3/kg. (broken grey line in Fig. 10, setting the K_d value to zero causes only a negligible additional increase of A_L/A_{tot}).

The wide range of K_d-values required to model the calcite data cannot be explained by variations of specific surface area only. This becomes clear when the data and model results for "ground calcite" (σ_0 = 3.9 m^2/g, K_d = 2.3 m^3/kg) are compared to those of rhombohedral calcite, which has a higher specific surface area (σ_0 = 7.7 m^2/g), yet require a much lower sorption coefficient (K_d = 0.08 m^3/kg) to fit the data. This example makes clear that the K_d-term includes, besides classical outer-sphere and inner-sphere surface adsorption, other fast surface-dominated isotope exchange processes occurring on "rough" surfaces with high defect and step densities. The magnitude of the K_d value can thus be taken as a measure of global surface reactivity, not limited to classical adsorption.

Complementary technical information and further calcite recrystallization data obtained in synthetic cement pore water (pH ≈ 13) by Curti et al. (2005) are given and discussed in S3.

3.6. Recrystallization rates from C(HOR) modeling compared with rates measured via AFM

The claim that the intrinsic recrystallization rate is related to

Fig. 9. [45]Ca activity data monitoring the recrystallization of different types of calcite, from Heberling et al. (2016), along with C(HOR) model best fits. Number in parentheses indicate the fitted recrystallization rates (R_e-values) in µmol m^{-2} d^{-1}.
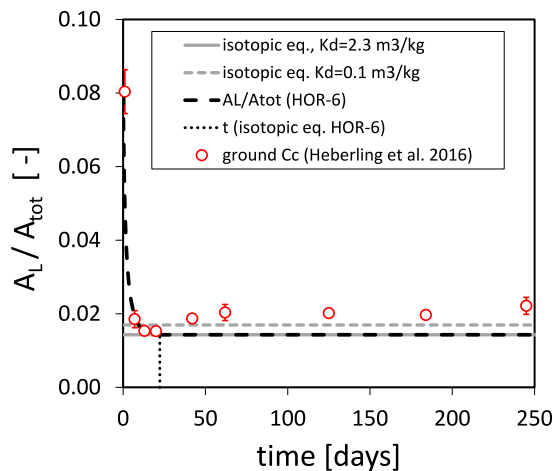

Fig. 10. [45]Ca tracer data for ground Iceland spar calcite (Heberling et al., 2016) compared with C(HOR) model results.

molecular scale kinetics (Section 2.4) can be tested by comparing the modeled R_e values with kinetic rates determined via atomic force microscopy (AFM). Baryte appears to be the most appropriate mineral for such a comparison, as in addition to systematic recrystallization data obtained at different experimental conditions for times extending to almost two years, also Atomic Force Microscopy (AFM) and other molecular to nanoscale studies exist for this mineral, against which our model results may be compared (Pina et al., 1998; Kuwahara et al., 2016; Bracco et al., 2016; Weber et al., 2017), albeit mostly carried out at low to moderate supersaturation. According to the Burton-Cabrera-Frank (BCF) theory (Burton et al., 1949), dissolution/precipitation proceeds at the molecular scale via detachment/attachment of single ions from/to the lattice of crystalline solids at favorable high-energy sites (so-called kink or half-position sites, see Markov, 1995). For baryte, AFM data show that at very low supersaturation the growth proceeds dominantly via spiral growth, which originates and propagates from screw dislocations (Pina et al., 1998; Kuwahara et al., 2016; Bracco et al., 2016; Weber et al., 2021). At high supersaturation, 2D-nucleation becomes dominant and growth rates increase.

Kuwahara et al. (2016) studied the growth kinetics of the (001) surface of a natural baryte as a function of supersaturation and found that both spiral growth and 2D-nucleation contribute to the total accretion of the solid at high supersaturation (SI ≥ 1). At lower supersaturation (SI = 0.5, i.e. closer to recrystallization conditions), growth rates decreased, with spiral growth becoming the dominant accretion mechanism. In Fig. 11 the data of Kuwahara et al. (2016) were plotted together with the effective recrystallization rates derived from the C (HOR) modeling of the baryte experiments illustrated in Fig. 4. It turns out that the R_e-value obtained for SL baryte in Ra-free solution after pre-equilibration (exp. A) apparently follows the exponential trend defined by the AFM data of Kuwahara et al. (2016) (showing up as a straight line in the doubly logarithmic plot) down to SI ≈ 0, suggesting an Arrhenius-type relation. The other two R_e values shown in Fig. 11 fall above the trend line, possibly indicating enhanced recrystallization kinetics induced by (a) the poor crystallinity and high surface energy contribution of untreated SL baryte (exp. 9) and (b) the catalyzing effect of radium in solution (exp. C). Although higher, the R_e-values from exp. 9 and exp. C are still considerably smaller than growth rates measured in supersaturated solutions.
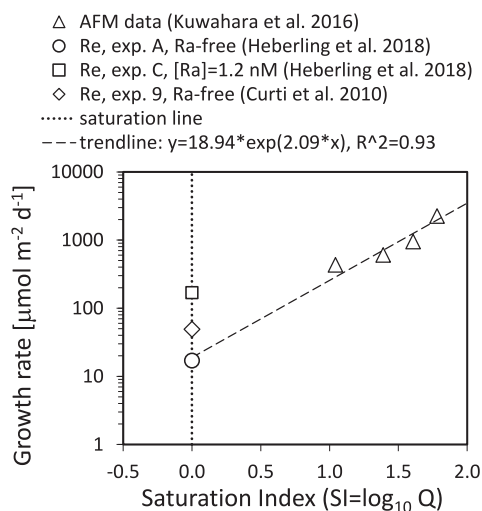

Fig. 11. AFM baryte growth rates in supersaturated solutions (triangles) (Kuwahara et al., 2016) compared to intrinsic recrystallization rates (R_e) extracted from C(HOR) model fits for SL baryte recrystallization experiments.

4. Discussion

4.1. Thermodynamic driving forces of D/P-driven recrystallization

The large differences in recrystallization kinetics and the distinct mechanisms (HOR vs. CHOR) involved in the tests with untreated and pre-equilibrated SL baryte in Ra-free solutions (exp. 9 and exp. A in Fig. 4, respectively) deserve a closer analysis. The reduction by a factor of two in specific surface area following pre-equilibration (from 0.31 to 0.15–0.17 m^2/g), attributed to the dissolution of small particulate material covering the initial surfaces of the untreated SL baryte particles, is insufficient to explain the dramatic change in macroscopic recrystallization rate observed after pre-equilibration. The modeling results discussed in Section 3.1 reveal that R_e-values after pre-equilibration for SL baryte are 2–3 times smaller than those derived for the same untreated baryte recrystallized under identical conditions (R_e = 17 vs. 49 μmol m^{-2} d^{-1}). The decrease in R_e appears to be correlated with an increase in crystallinity during the pre-equilibration in the aqueous solution, as revealed by the XRD-data (Heberling et al., 2018). Indeed, Rietveld refinement showed a narrowing of the Bragg reflection peaks, pointing to an increase in average crystal domain size (from 220 to 320 nm), as well as a strong decrease in the Debye-Waller factors for S and O, indicating increased near-range ordering.

The XRD results indicate structural changes in the entire volume of the solid, implying that during the pre-equilibration process the aqueous solution had access to the bulk volume of the primary solid, which seems only possible if an open internal porosity was present from the start to the end of the pre-equilibration process. The characterization data of Weber et al. (2016, 2017) confirm that a pervasive nanoporosity was still present in SL baryte pre-equilibrated in Ra-free solution (see Section 3.1).

In summary, the combined data of Curti et al. (2010); Heberling et al. (2018); Brandt et al. (2015) and Weber et al. (2016, 2017) suggest the following picture for the observed kinetic evolution of SL baryte in Ra-free water: (a) the free energy excess of the external particle surfaces in the untreated SL baryte (due to the combined effect of defects, attached nanoparticles and poor crystallinity) favors the observed rapid initial [133]Ba uptake. This process is complete within a single day and limited to the top 1–2 monolayers and can thus be modeled as surface adsorption process by assuming K_d = 0.3 m^3/kg. (b) Between 1 and 200 days the aqueous solution penetrates into the interior of the particles via pre-existing micro- and nanoporosity. The free energy excess arising from the internal pore surfaces is annealed at a faster rate compared to the progression of the recrystallization front. The water penetration rate thus controls the recrystallization kinetics, explaining why this stage can be reproduced assuming the HOR mechanism. (c) After 200 days, which roughly corresponds to the pre-equilibration time in the experiments of Heberling et al. (2018), the untreated SL baryte has been *completely* transformed into a more crystalline product with much lower surface free energy. Even if an internal porosity still exists, the recrystallization kinetics becomes slow, as any further decrease in free energy requires dissolution-reprecipitation of progressively larger coherent domains compared to the untreated SL baryte. In the long term, this happens via repeated, progressively slower cycles, as postulated through the CHOR mechanism.

The systematic study of Heberling et al. (2016) yields further insight on the driving forces of D/P-recrystallization. By monitoring the [45]Ca removal from solution on different types of natural and commercial calcites under the same initial conditions (pH = 8.2, 0.01 M NaCl, 5 g/l, room temperature) and by measuring the short-term increase in calcite solubility of ground Iceland spar, it was possible to split the contributions of flat crystal faces and surface roughness to the total surface energy. Mathematically, this was formulated in an extended version of Schindler's equation (Schindler, 1967), in which "surface roughness" is treated as an additional surface tension term (expressed as δ [J m^{-2}]). This term includes the contribution of defects present on the uneven

crystal surfaces (such as steps and screw dislocations) and adds to the conventional term defined by the interfacial tension of a specific ideal crystal face 'i' (γ_i [J m^{-2}]) in the aqueous solution of interest. Using the extended equation and correlating it with the observed ^{45}Ca uptake, three major different driving forces could be identified that correlate with the observed recrystallization kinetics: (a) the fast spontaneous decrease in "surface roughness", leading to more euhedral form for a given crystal habitus; (b) the tendency for transformation of an initial habitus with comparatively high surface tension to a more stable one of lower surface tension (the order of stability being for calcite: rhombohedral > scalenohedral > prismatic); and (c) the reduction of total surface free energy via crystal growth at the expense of small particles (Ostwald ripening *s.s.*).

The influence of surface defects at the water/mineral interface was clearly demonstrated in a seminal study by Schott et al. (1989) who observed increased dissolution kinetics on strained calcites with increasing density of dislocations. However, the increase in dissolution rate was asymmetrical, i.e. small (by a factor of two-three) compared to the corresponding increase in defect density (three orders of magnitude). Moreover, a critical threshold density seemed necessary to induce a measurable enhancement in dissolution rate. Whether such effects can be extended to precipitation and recrystallization kinetics is not clear, as comparable measurements as a function of defect density are not available in supersaturated or saturated solutions to the knowledge of the authors. Nevertheless, it is well-known from crystal theory (Burton et al., 1949) that heterogeneous nucleation from supersaturated solutions is favored at kink sites originating at screw dislocation, as for dissolution. Therefore similar effects are likely, although not necessarily "symmetrical", also for precipitation and recrystallization.

A further thermodynamic driving force for recrystallization (d) is the presence of a chemical potential gradient when a foreign trace element added to the solution forms a solid solution with the initially pure recrystallizing solid. In this case, the initial aqueous solution is in "perfect" saturation equilibrium with the primary pure solid, but is slightly supersaturated with respect to the (not yet formed) solid solution. Once formation of the solid solution starts, typically favored by heterogeneous nucleation on the surface of the primary solid (Poonoosamy et al., 2016), the aqueous phase adjacent to the nascent solid solution becomes undersaturated with respect to the primary solid, due to the decrease in local concentrations of the carrier ions (e.g., Ba^{2+} and SO$_4^{2-}$ in the case of baryte). This leads to local concentration gradients that drive the dissolution of the primary pure solid and further growth of the solid solution. Any of the aforementioned driving forces may be blocked at any time during the recrystallization process if the internal porosity structure "closes" preventing the access of aqueous solution to more internal non-recrystallized domains.

A fifth recrystallization driving force specific to minerals containing redox-sensitive elements (e) has been found to operate in Fe oxyhydroxides. In the presence of dissolved Fe(II), complete Fe isotope exchange was shown to occur at a very fast rate (within a few weeks) in nanoparticulate goethite, in spite of no obvious change in crystal morphology and scarce evidence for internal porosity. Handler et al. (2009, 2014) proposed electron conduction to be pathway for such an "Fe(II)-catalyzed atom exchange" process. Accordingly, Fe(II) would first adsorb on the surface of the goethite particles, however with different crystal face-dependent site densities. This would lead different surface charges on specific faces and thus create an electric potential across them, which acts as driving force for electron transfer through the solid (a "redox-driven conveyor belt" in the terminology of Handler et al., 2009). Such a mechanism does not require any internal porosity, only electron transfer. The solid dissolves on the electron acceptor surface, where the Fe^{3+} of the goethite lattice is reduced to soluble Fe^{2+}, and grows on the electron donor surface, where the Fe^{2+} adsorbed from the aqueous solution is oxidized to sparingly soluble Fe^{3+}, which is incorporated into newly formed goethite. The fact that no obvious change was observed in the morphology of the goethite particles, all

strongly elongated parallel to the c-axis, was explained by Handler et al. (2009) by assuming that the electric potential runs across faces parallel to the c-axis.

4.2. Comparison of C(HOR) and "back-reaction" recrystallization models

The model fits shown in Fig. 6 and Fig. 7 for the Fe-isotope exchange data on goethite recrystallization (Joshi et al., 2017; Joshi et al., 2022; Frierdich et al., 2015a) indicates that C(HOR) performs equally well as the "back reaction" model of Joshi et al. (2022). This prompts for an in-depth comparison of the two models, with focus on the parametrization and the information that can be gained from either model.

As in C(HOR), Joshi et al. (2022) assumed that recrystallization proceeds via a D/P process. A key concept in their model is that of "back-reaction", defined as "*the fraction of the recrystallized solid that further dissolves and reprecipitates*". We understand this as the fraction that continues to recrystallize after it has undergone a first D/P cycle. This concept is analogous to the repeated D/P cycles postulated in the CHOR model and similarly introduces a retardation of the macroscopic recrystallization kinetics, however it lacks any assumption on physical geometry of the particles and the advancement of the recrystallization front.

In their formulation, Joshi et al. (2022) assume that the observed macroscopic recrystallization rate can be computed by summing up two exponential time-dependent terms simulating the initially fast (but short-lived) recrystallization and a slower, gradual "back-reaction" that operates in parallel. The model is parametrized using, for each of the two rates (*fast* and *slow)* two empirical constants a, b in the exponential equation $r_{fast,slow} = a_{fast,slow} \bullet exp(t/b_{fast,slow})$, yielding two time-dependent rates r_{fast} and r_{slow}, the sum of which defines the macroscopically observed rate (r). We use here lowercase 'r' to indicate that these rates are not normalized to the exposed surface area, contrary to the formulation in the C(HOR) models. According to the definitions given in Joshi et al. (2022) $r(t)$ has to be understood as instantaneous rate that can be easily converted to $R_i(t)$ by division with the exposed surface area, S_0.

In the case of the ^{55}Fe data illustrated in Fig. 6, an initial recrystallization rate of 4.04 μmol m^{-2} d^{-1} ($r/S_0 = R_i = R_e$ at $t = 0$) can be extracted from the data of Joshi et al. (2022) that compares well with the intrinsic recrystallization rate ($R_e = 4.3$ μmol m^{-2} d^{-1}) determined with our HOR model best-fit for the first 30 days. In Joshi's formalism, the recrystallization rate then gradually decreases by three orders of magnitude down to $r/S_0 = R_i = 4.72 \times 10^{-3}$ μmol m^{-2} d^{-1} at the end of the experiment. The same kinetic behavior was simulated with our modeling approach, however assuming two distinct consecutive recrystallization mechanisms, each with a specific effective recrystallization rate: $R_e = 4.3$ μmol m^{-2} d^{-1} with HOR for non-aged goethite ("first spiking"); and $R_e = 0.034$ μmol m^{-2} d^{-1} with CHOR after 30 days pre-equilibration ("second spiking").

So far, we have shown that the two models yield equivalent good fits of the experimental data and similar macroscopic rates. In the next step, the two models are compared in terms of the information gained and the practical use of the extracted best fit parameters. The "back-reaction" model is purely empirical as it requires, to reproduce the observed macroscopic kinetics, four freely adjustable fitting parameters (a_{slow}, b_{slow}, a_{fast}, b_{fast}) unrelated to any physical-chemical property. This scheme allows for a large flexibility in reproducing tracer uptake kinetics curves, however it yields purely descriptive model results in the form of r_{slow} and r_{fast} (the sum of which yields r).

In contrast, the C(HOR) approach attempts to extract, in addition to macroscopic rates, a more fundamental kinetic parameter, the effective (intrinsic) recrystallization rate (R_e), which we interpreted as the rate of dissolution/re-precipitation *at the molecular scale of a single monolayer*. The "cost" for obtaining such information is (a) the need to measure or

estimate a number of physical-chemical parameters (specific surface area, solid to liquid ratio, monolayer thickness, carrier element concentration) for the system of interest and (b) to impose model-consistent experimental constraints. Only when such pre-requisites are fulfilled and verified can the fitted R_e and K_d (the remaining freely adjustable parameters) be considered to yield veritable geochemical information. Actually, if the first measurement of tracer activity in solution occurs within 1 day after spiking, the fitted K_d can be considered as independently measured fixed parameter, leaving R_e as unique fit parameter.

A critical C(HOR) model constraint is the carrier element concentration, C_s, which is required to be constant within narrow limits, since thermodynamic saturation equilibrium is a necessary condition for recrystallization to occur. The constancy of C_s must be verified experimentally not only as a proof that close-to-saturation conditions are maintained during the entire experiment, but also because the calculated recrystallization rates proved to be very sensitive to this parameter. The "back reaction" model does not require such constraints, however the obtained recrystallization rates could be strongly biased by net dissolution or precipitation if C_s varies during the experiment.

Another key parameter in C(HOR) is the monolayer thickness, d, which is inversely correlated to R_e, see Eq. (5). Because there is always some degree of judgment in selecting a monolayer thickness value (d), this parameter is affected by a considerable uncertainty, which necessarily propagates to R_e. Based on a simple estimation, we conclude that the uncertainty of R_e introduced by the "subjectivity" of d-values is limited to ± 0.7 $\log_{10}$ units (see S3 for details).

A final question to address is why in some cases HOR and in other cases CHOR is the appropriate formalism describing recrystallization. From the analysis of the available data, it appears that HOR prevails in recrystallization processes involving solids with a high surface free energy excess, i.e. typically in suspensions of non pre-equilibrated, poorly crystalline solids with large specific surface area and a high density of structural defects. In such cases one observes initially a fast (quasi-instantaneous) decrease of the tracer in solution, followed by isotope homogenization at a rate frequently limited by the penetration rate of the spiked solution into the interior of the porous solid particles. After the first HOR-cycle is completed, recrystallization usually continues via multiple dissolution/re-precipitation cycles. Not only the bulk recrystallization rate, also the effective recrystallization rate, R_e, is in general smaller at this stage, since the solid has already reduced its surface free energy excess, either through annealing of surface defects or increasing the size of crystallites, in the preceding HOR cycle.

An exception to the above picture are C-S-H phases, which in spite of the high surface area and poor crystallinity follow from the start on the CHOR pathway. This may be related to the fact that C-S-H phases are actually solid solutions that continuously adjust their stoichiometry (Ca: Si ratio) to the aqueous phase composition.

4.3. Effect of solubility product and ionic ratio on recrystallization kinetics

Recrystallization rates may also depend on solution composition. In analogy with precipitation from supersaturated solutions, one expects a dependence both on the solubility product (Curti, 1997; Curti, 1999) and on the ratio of the recrystallizing mineral's constituent ions. For baryte, maximum growth rates in supersaturated solutions are expected at Ba:SO$_4$ = 1 (Kowacz et al., 2007; Bracco et al., 2016) when both Ba^{2+} and SO_4^{2-} concentrations are close to equimolarity at $\approx 10^{-5}$ M (since $K_{sp}^0 = 10^{-9.96}$, see Brown et al., 2019). At lower or higher Ba:SO$_4$ ratios, the saturation concentration of either Ba^{2+} or SO_4^{2-} would obviously be less than 10^{-5} M. Thus, the supply of one of the two constituents is reduced and therefore the growth rate is smaller than in otherwise identical equimolar solutions.

In Fig. 12, all the R_e-values extracted via C(HOR) modeling in the present paper have been plotted as a function of the carrier element concentration in the aqueous phase. As expected from the variety of
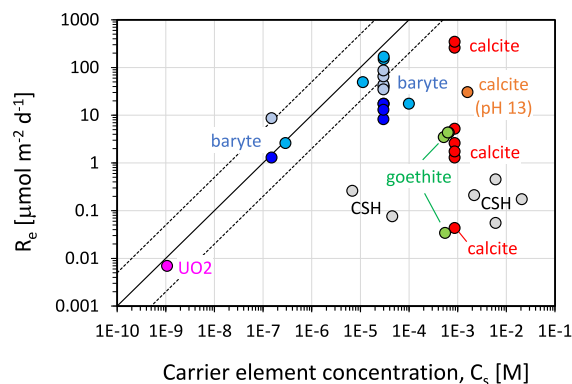
Fig. 12. Plot showing the effective recrystallization rates (R_e) obtained via C (HOR) modeling as a function of the carrier element concentration in solution, C_s (Ca for C-S-H and calcite, Ba for baryte, Fe for goethite, U for UO$_2$) for experimental data extracted from various mineral recrystallization studies. See text for the meaning of the broken and solid bounding lines.

driving forces and solid phases involved, as well as from the widely different experimental conditions, the data scatter considerably, even for a single mineral. Nevertheless, a correlation trend with approximately 1:1 slope is detected between C_s and R_e, defined by the baryte data and UO$_2$ (solid line, the broken lines defining estimated R_e-uncertainties of ± 0.7 $\log_{10}$ units). As a working hypothesis to be verified in future studies, we propose that this trend may represent the upper limit of achievable R_e–values (at any given carrier element concentration, C_s). This may arise from mass transfer limitations, e.g. diffusive fluxes of solutes between dissolving and growing solid (e.g. during Ostwald ripening) which will tend to be smaller if the recrystallizing mineral is sparingly soluble, compared to more soluble solids.

Some of the baryte data in Fig. 12 align along this trend and seem to be consistent with this explanation, according to the previously discussed dependence of baryte growth rates on the Ba:SO$_4$ ratio in solution. Indeed, at $C_s = $[Ba] =$10^{-6}$–$10^{-7}$ M (Ba:SO$_4 \approx 10^{-3}$–10^{-4}) R_e is 1–2 orders of magnitude lower compared to the other baryte data clustering at $C_s \approx 10^{-5}$ (Ba:SO$_4 \approx 1$). UO$_2$, by far least soluble solid among those considered in this review ($C_s = $[U] $\approx 10^{-9}$–10^{-10} M), has as expected by far the lowest recrystallization rate of all analyzed minerals and falls close to the postulated boundary.

4.4. Integrated C(HOR) results

In Fig. 13 further model results associated to the fits presented in Fig. 4 through Fig. 10 are shown, giving a synthesis of the C(HOR) model output across several minerals. Fig. 13a shows percentages of primary solid recrystallized as a function of solid/water interaction time, obtained by applying Eq. (7) (HOR) or Eq. (11) (CHOR) after dividing by the initial amount of solid, n_0. Fig. 13b presents the corresponding instantaneous recrystallization rates, R_i, derived from Eq. (14) (HOR) or Eq. (15) (CHOR). The two figures exemplify the richness of information and flexibility offered by the C(HOR) formalism, allowing the compact representation of multiple model results on a single graph.

Specifically, the plots in Fig. 13a reveal that while in some tests macroscopic recrystallization is so fast to reach isotopic equilibrium within a few weeks via HOR mechanism, in other tests only small to moderate fractions of the primary solid has recrystallized after more than one year, due to slow R_e rates combined with the CHOR recrystallization pathway. Consequently, the R_i plots in Fig. 13b show large variations of the instantaneous recrystallization rates even for the same mineral, according to the driving forces operating in each experiment.
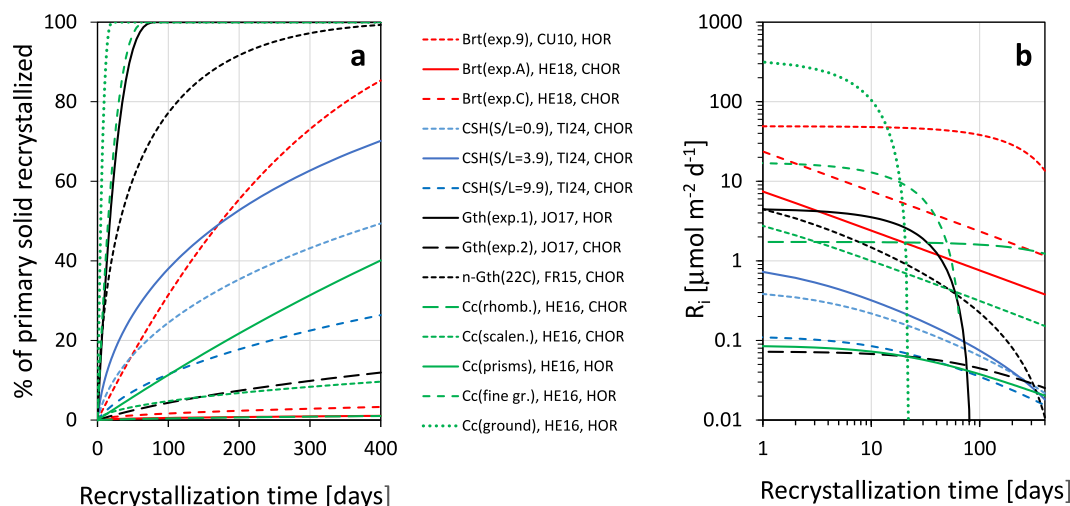
Fig. 13. Percentages of primary solid recrystallized (a) and instantaneous recrystallization rates (b) derived from the C(HOR) model, corresponding to fits shown in Fig. 4 through Fig. 10. Legend key: Brt = baryte, CSH = calcium silicate hydrate, Gth = goethite, Cc = calcite., with experiment identification in parentheses. References: CU10= Curti et al. (2010), HE18= Heberling et al. (2018), TI24= Tits et al. (2024), JO17= Joshi et al. (2017), FR15= Frierdich et al. (2015a), HE16= Heberling et al. (2016).

5. Summary and conclusions

This study provides a mathematical formulation of the HOmogeneous Recrystallization (HOR) and Continuous HOmogeneous Recrystallization (CHOR) models, both coupled to instantaneous reversible adsorption via a K_d approach. The models were applied to fit published (radio)tracer uptake data in order to derive recrystallization rates of various minerals in aqueous solution (baryte, calcite, calcium-silicate hydrates, goethite, and uranium(IV) dioxide).

The modeling results, in combination with available microscopic characterization data, enabled us to identify the driving forces controlling D/P-driven recrystallization. These include: (1) the reduction of surface energy excess arising from a high density of defects (kink sites, dislocations, steps) and/or a high initial specific surface area; (2) the transformation of an initially amorphous or poorly crystalline solid into a more stable crystalline solid (increase in crystallite size; transformation into a more stable habitus); (3) the annealing of chemical potential gradients when foreign trace elements are incorporated into the recrystallized solid as solid solution; (4) the annealing of electric potential gradients in redox active solids (Fe oxy-hydroxides).

The modeling also allowed us to correlate, to some extent, recrystallization mechanisms with driving forces. HOR was found to prevail in recrystallization processes involving solids with a high surface free energy excess, i.e. typically in suspensions of untreated, poorly crystalline solids with high specific surface area. In contrast, the CHOR mechanism is typical of minerals that have reached a higher degree of maturity (higher crystallinity) via long-term pre-equilibration in aqueous solution.

Our review and modeling demonstrate that mineral recrystallization in aqueous solutions is a complex phenomenon driven by multiple mechanisms correlated to chemical-physical properties of the primary solid (e.g. density of surface defects, presence or absence of accessible internal porosity). The variety of recrystallization driving forces results in diverse effects depending on the nature of the involved solids and environmental conditions, ranging from complete exchange of ions in the solid within a few days to long-term metastability. Accurate predictions on kinetics and extent of recrystallization are thus possible only after a precise characterization of the initial solids down to the molecular scale and knowledge of environmental conditions.

CRediT authorship contribution statement

Enzo Curti: Writing – original draft, Validation, Formal analysis, Data curation, Conceptualization. **Jan Tits:** Data curation, Conceptualization. **Frank Heberling:** Writing – review & editing, Data curation, Conceptualization.

Declaration of competing interest

The authors declare that they have no known competing financial interests or personal relationships that could have appeared to influence the work reported in this paper.

Appendix A. Supplementary data

Supplementary data to this article can be found online at https://doi.org/10.1016/j.chemgeo.2025.123169.

Data availability

Data and model results are available online at the following sharing link: https://data.mendeley.com/preview/cr5ckvdffy?a=fb442fd6-54f1-4642-9e6d-0933a90f56e2.

References

Beck, J.W., Berndt, M.E., Seyfried, W.E., 1992. Application of isotopic doping techniques to evaluation of reaction kinetics and fluid/mineral distribution coefficients: an experimental study of calcite at elevated temperatures and pressures. Chem. Geol. 97 (1), 125–144.

Bethke, C.M., 2022. Kinetics of dissolution and precipitation. In: Geochemical and Biogeochemical Reaction Modeling, 3rd ed. Cambridge University Press, pp. 515–550.

Boistelle, R., Astier, J.P., 1988. Crystallization mechanisms in solution. J. Cryst. Growth 90, 14–30.

Bracco, J.N., Grantham, M.C., Stack, A.G., 2012. Calcite growth rates as a function of aqueous calcium-to-carbonate ratio, saturation index, and inhibitor concentration:

insight into the mechanism of reaction and poisoning by strontium. Cryst. Growth Des. 12, 3540–3548.

Bracco, J.N., Gooijer, Y., Higgins, S.R., 2016. Hydrothermal atomic force microscopy observations of barite step growth rates as a function of the aqueous barium-to-sulfate ratio. Geochim. Cosmochim. Acta 183, 1–13.

Brandt, F., Curti, E., Klinkenberg, M., Rozov, K., Bosbach, D., 2015. Replacement of barite by a (Ba,Ra)SO$_4$ solid solution at close-to-equilibrium conditions: a combined experimental and theoretical study. Geochim. Cosmochim. Acta 155, 1–15. https://doi.org/10.1016/j.gca.2015.01.016.

Brandt, F., Klinkenberg, M., Poonoosamy, J., Bosbach, D., 2020. Recrystallization and uptake of ^{226}Ra into Ba-rich (Ba,Sr)SO$_4$ solid solutions. Minerals 10, 812.

Brown, P.L., Ekberg, C., Matyskin, A.V., 2019. On the solubility of radium and other alkaline earth sulfate and carbonate phases at elevated temperature. Geochim. Cosmochim. Acta 255, 88–104.

Burton, K., Cabrera, N., Frank, F.C., 1949. The growth of crystals and the equilibrium structure of their surfaces. In: Phil. Trans. R. Soc. London, Ser. A: Mathematical, Physical and Engineering Sciences, 243(866), pp. 299–358.

Busenberg, E., Plummer, L.N., 1986. A comparative study of the dissolution and crystal growth kinetics of calcite and aragonite. In: Mumpton, F.A. (Ed.), Studies in Diagenesis, 1578. U.S. Geological Survey Bull, pp. 139–168.

Camacho Meneses, G.C., Weber, J., Hermann, R.P., Wanhala, A., Stubbs, J.E., Eng, P.J., Borisevich, A.Y., Boebinger, G., Liu, T., Stack, A.G., Bracco, J.N., 2025. Inhibition of reaction layer formation on MgO(100) by doping with trace amounts of iron. J. Phys. Chem. C 129, 3457–3468.

Chanda, P., Fantle, M.S., 2017. Quantifying the effect of diagenetic recrystallization on the Mg isotopic composition of marine carbonates. Geochim. Cosmochim. Acta 204, 219–239.

Cross, A.J., Skemer, P., 2019. Rates of dynamic recrystallization in geologic materials. J. Geophys. Res. Solid Earth 124, 1324–1342. https://doi.org/10.1029/2018JB016201.

Curti, E., 1997. Coprecipitation of radionuclides: basic concepts, literature review and first applications. In: Technical Report NTB 97-08, National Cooperative for the Disposal of Radioactive Waste (Nagra), Wettingen, Switzerland. https://nagra.ch/downloads/technical-report-ntb-97-08/.

Curti, E., 1999. Coprecipitation of radionuclides with calcite: estimation of partition coefficients based on a review of laboratory investigations and geochemical data. Appl. Geochem. 14, 433–445.

Curti, E., Kulik, D.A., Tits, J., 2005. Solid solutions of trace Eu(III) in calcite: thermodynamic evaluation of experimental data over a wide range of pH and pCO$_2$. Geochim. Cosmochim. Acta 69 (7), 1721–1737.

Curti, E., Fujiwara, K., Iijima, K., Tits, J., Cuesta, C., Kitamura, A., Glaus, M.A., Müller, W., 2010. Radium uptake during barite recrystallization at 23 +/− 2 °C as a function of solution composition: an experimental Ba-133 and Ra-226 tracer study. Geochim. Cosmochim. Acta 74, 3553–3570.

Davis, K.J., Dove, P.M., De Yoreo, J.J., 2000. The Role of Mg^{2+} as an impurity in calcite growth. Science 290 (5494), 1134–1137.

De Yoreo, J.J., Zepeda-Ruiz, L.A., Friddle, R.W., Qiu, S.R., Wasylenki, L.E., Chernov, A.A., Gilmer, G.H., Dove, P.M., 2009. Rethinking classical crystal growth models through molecular scale insights: consequences of kink-limited kinetics. Cryst. Growth Des. 9 (12), 5135–5144.

De Yoreo, J.J., Gilbert, P.U., Sommerdijk, N.A., et al., 2015. Crystallization by particle attachment in synthetic, biogenic, and geologic environments. Science 349 (6247), aaa6760.

Di Lorenzo, F., Ruiz-Agudo, C., Churakov, S.V., 2019. The key effects of polymorphism during Pb^{II} uptake by calcite and aragonite. Cryst. Eng. Comm. 21, 6145.

Di Lorenzo, F., Arnold, T., Churakov, S.V., 2021. Pb^{2+} uptake by magnesite: the competition between thermodynamic driving force and reaction kinetics. Minerals 11, 415. https://doi.org/10.3390/min11040415.

Doerner, H.A., Hoskins, W.M., 1925. Co-precipitation of radium and barium sulphates. J. Am. Chem. Soc. 47, 662–675.

Enüstün, B.V., Turkevich, J., 1960. Solubility of fine particles of strontium sulfate. J. Am. Chem. Soc. 82, 4502–4509.

Frierdich, A.J., Catalano, J.G., 2011. Controls on Fe(II)-activated trace element release from goethite. Environ. Sci. Technol. 2012 (46), 1519–1526.

Frierdich, A.J., Beard, B.L., Reddy, T.R., Scherer, M.M., Johnson, C.M., 2014a. Iron isotope fractionation between aqueous Fe(II) and goethite revisited: New insights based on a multi-direction approach to equilibrium and isotopic exchange rate modification. Geochim. Cosmochim. Acta 139, 383–398.

Frierdich, A.J., Beard, B.L., Scherer, M.M., Johnson, C.M., 2014b. Determination of the Fe(II)aq- magnetite equilibrium iron isotope fractionation factor using the three isotope method and a multi-direction approach to equilibrium. Earth Planet. Sci. Lett. 391, 77–86.

Frierdich, A.J., Beard, B.L., Rosso, K.M., Scherer, M.M., Spicuzza, M.J., Valley, J.W., Johnson, C.M., 2015a. Low temperature, non-stoichiometric oxygen-isotope exchange coupled to Fe(II) – goethite interactions. Geochim. Cosmochim. Acta 160, 38–54.

Frierdich, A.J., Helgeson, M., Liu, C., Wang, C., Rosso, K.M., Scherer, M.M., 2015b. Iron atom exchange between hematite and aqueous Fe(II). Environ. Sci. Technol. 49 (14), 8479–8486.

Frierdich, A.J., Nebel, O., Beard, B.L., Johnson, C.M., 2019a. Iron isotope exchange and fractionation between hematite α-Fe$_2$O$_3$ and aqueous Fe(II): a combined three-isotope and reversal-approach to equilibrium study. Geochim. Cosmochim. Acta 245, 207–221.

Frierdich, A.J., Saxey, D.W., Adineh, V.R., Fougerouse, D., Reddy, S.M., Rickard, W.D.A., Sadek, A.Z., Southall, S.C., 2019b. Direct observation of nanoparticulate goethite recrystallization by atom probe analysis of isotopic tracers. Environ. Sci. Technol. 53 (22), 13126–13135 (PMID: 31657213).

Gorski, Ch.A., Fantle, M.S., 2017. Stable mineral recrystallization in low temperature aqueous systems: a critical review. Geochim. Cosmochim. Acta 198, 439–465.

Handler, R.M., Beard, B.L., Johnson, C.M., Scherer, M.M., 2009. Atom exchange between aqueous Fe(II) and goethite: an Fe isotope tracer study. Environ. Sci. Technol. 43, 1102–1107.

Handler, R.M., Frierdich, A.J., Johnson, C.M., Rosso, K.M., Beard, B.L., Wang, C., Latta, D.E., Neumann, A., Pasakarnis, T., Premaratne, W.A.P.J., Scherer, M.M., 2014. Fe(II)-catalyzed recrystallization of goethite revisited. Environ. Sci. Technol. 48, 11302–11311.

Heberling, F., Paulig, L., Nie, Z., Schild, D., Finck, N., 2016. Morphology controls on calcite recrystallization. Environ. Sci. Technol. 50, 11735–11741.

Heberling, F., Metz, V., Böttle, M., Curti, E., Geckeis, H., 2018. Barite recrystallization in the presence of ^{226}Ra and ^{133}Ba. Geochim. Cosmochim. Acta 232, 124–139.

Henderson, L.M., Kracek, F.C., 1927. The fractional precipitation of barium and radium chromates. J. Amer. Chem. Soc. 49, 739–749.

Hoffmann, T.D., Reeksting, B.J., Gebhard, S., 2021. Bacteria-induced mineral precipitation: a mechanistic review. Microbiology 167, 001049. https://doi.org/10.1099/mic.0.001049.

Joshi, P., Fantle, M.S., Larese-Casanova, P., Gorski, C.A., 2017. Susceptibility of goethite to Fe^{2+}-catalyzed recrystallization over time. Environ. Sci. Technol. 51 (20), 11681–11691.

Joshi, P., Fantle, M.S., Boualavong, J., Gorski, Ch.A., 2022. Quantifying the rate of Fe^{2+}-catalyzed recrystallization based on a unifying model framework. Geochim. Cosmochim. Acta 336, 423–435.

Kahlweit, M., 1975. Ostwald ripening of precipitates. Adv. Colloid Interf. Sci. 5, 1–35.

Kowacz, M., Putnis, C.V., Putnis, A., 2007. The effect of cation:anion ratio in solution on the mechanism of barite growth at constant supersaturation: role of the desolvation process on the growth kinetics. Geochim. Cosmochim. Acta 71, 5168–5179.

Kurganskaya, I., Lüttge, A., 2024. Probability distributions of mineral dissolution rates: the role of lattice defects. Front. Water 5, 1225837.

Kuwahara, Y., Liu, W., Makio, M., Otsuka, K., 2016. In Situ AFM study of crystal growth on a Barite (001) surface in BaSO$_4$ solutions at 30 °C. Minerals 6, 117. https://doi.org/10.3390/min6040117.

Lasaga, A.C., 2014. Kinetic Theory in the Earth Sciences. Princeton University Press, Princeton. https://doi.org/10.1515/9781400864874.

Markov, I.V., 1995. Crystal Growth for Beginners: Fundamentals of Nucleation, Crystal Growth, and Epitaxy. World Scientific, Singapore.

Marques Fernandes, M., Baeyens, B., Bradbury, M.H., 2008. The influence of carbonate complexation on lanthanide/actinide sorption on montmorillonite. Radiochim. Acta 96, 691–697. https://doi.org/10.1524/ract.2008.1555.

McIntire, W.L., 1963. Trace element partition coefficients – a review of theory and applications to geology. Geochim. Cosmochim. Acta 27, 1209–1264.

Metz, R., Kumar, N., Schekeveld, W.D.C., Kraemer, S.M., 2023. Rates and mechanism of vivianite dissolution under anoxic conditions. Environ. Sci. Technol. 57, 17266–17277.

Nagy, K.L., Lasaga, A.C., 1992. Dissolution and precipitation kinetics of gibbsite at 80°C and pH 3: the dependence on solution saturation state. Geochim. Cosmochim. Acta 56, 3093–3111.

Navrotsky, A., 2009. Mineral precipitation kinetics. Rev. Mineral. Geochem. 70 (1), 371–410.

Nielsen, L.C., DePaolo, D.J., De Yoreo, J.J., 2012. Self-consistent ion-by-ion growth model for kinetic isotopic fractionation during calcite precipitation. Geochim. Cosmochim. Acta 86, 166–181.

Olilla, K., 2006. Dissolution of Unirradiated UO$_2$ and UO$_2$ Doped with ^{233}U in 0.01 M NaCl under Anoxic and Reducing Conditions. Report 2006-08, Posiva Oy, Fin – 27160, Olkiluoto, Finland.

Olilla, K., 2008. Dissolution of unirradiated UO$_2$ and UO$_2$ doped with ^{233}U in low- and high-ionic-strength NaCl under anoxic and reducing conditions. In: Working Report 2008–50, Posiva Oy, Fin – 27160, Olkiluoto, Finland.

Pina, C.M., Becker, U., Risthaus, P., Bosbach, D., Putnis, A., 1998. Molecular-scale mechanisms of crystal growth in barite. Nature 395, 483–486.

Pokrovsky, O.S., Schott, J., 2004. Experimental study of brucite dissolution and precipitation in aqueous solutions: surface speciation and chemical affinity control. Geochim. Cosmochim. Acta 68 (1), 31–45.

Poonoosamy, J., Curti, E., Kosakowski, G., Van Loon, L.R., Grolimund, D., Mäder, U., 2016. Barite precipitation following celestite dissolution in a porous medium: a SEM/ BSE and micro XRF/XRD study. Geochim. Cosmochim. Acta 182, 131–144.

Prior, D.J., Bestmann, M., Halfpenny, A., Mariani, E., Piazolo, S., Tullis, J., Wheeler, J., 2004. Recrystallization and grain growth in rocks and minerals. Mater. Sci. Forum 467–470, 545–550.

Putnis, A., 2009. Mineral Replacement Reactions. Rev. Mineral. Geochem. 70, 87–124.

Putnis, A., 2015. Transient porosity resulting from fluid–mineral interaction and its consequences. Rev. Mineral. Geochem. 80, 1–23.

Putnis, A., Putnis, C.V., 2007. The mechanism of reequilibration of solids in the presence of a fluid phase. J. Solid State Chem. 180 (5), 1783–1786.

Putnis, Ch.V., Ruiz-Agudo, E. (Eds.), 2013. The mineral-water interface. Elements 9 (3).

Ruiz-Agudo, E., Putnis, C.V., Putnis, A., 2014. Coupled dissolution–precipitation at mineral–fluid interfaces. Chem. Geol. 383, 132–146. https://doi.org/10.1016/j.chemgeo.2014.06.007.

Schindler, P.W., 1967. Heterogeneous equilibria involving oxides, hydroxides, carbonates, and hydroxide carbonates. In: Stumm, W. (Ed.), Equilibrium Concepts in Natural Water Systems. Advances in Chemistry, A. Chem. Soc, Washington DC, pp. 196–221.

Schott, J., Brantley, S., Crerar, D., Guy, Ch., Borksik, M., Willaime, Ch., 1989. Dissolution kinetics of strained calcite. Geochim. Cosmochim. Acta 53, 373–382.

Sugimoto, T., 2019. Monodispersed Particles, 2nd edition. Elsevier, Amsterdam (NL), p. 826.

Tadros, T., 2013. Ostwald ripening. In: Tadros, T. (Ed.), Encyclopedia of Colloid and Interface Science. Springer, Berlin, Heidelberg. https://doi.org/10.1007/978-3-642-20665-8_12.

Taylor, S.D., Liu, J., Zhang, X., Arey, B.W., Kovarik, L., Schreiber, D.K., Perea, D.E., Rosso, K.M., 2019. Visualizing the iron atom exchange front in the Fe(II)-catalyzed recrystallization of goethite by atom probe tomography. Proc. Natl. Acad. Sci. 116 (8), 2866–2874.

Tits, J., Curti, E., Laube, A., Wieland, E., Provis, J., 2024. Sorption of ^{32}Si and ^{45}Ca by isotopic exchange during; recrystallization of cement phases. Appl. Geochem. 173, 106117.

Tsukamoto, K., 2016. In-situ observation of crystal growth and the mechanism. Prog. Cryst. Growth Charact. Mater. 62, 111–125.

Vinograd, V.L., Kulik, D.A., Brandt, F., Klinkenberg, M., Weber, J., Winkler, B., Bosbach, D., 2018a. Thermodynamics of the solid solution - aqueous solution system (Ba,Sr,Ra)SO$_4$ + H$_2$O: I. the effect of strontium content on radium uptake by barite. Appl. Geochem. 89, 59–74. https://doi.org/10.1016/j.apgeochem.2017.11.009.

Vinograd, V.L., Kulik, D.A., Brandt, F., Klinkenberg, M., Weber, J., Winkler, B., Bosbach, D., 2018b. Thermodynamics of the solid solution - Aqueous solution system (Ba,Sr,Ra)SO$_4$ + H$_2$O: II. Radium retention in barite-type minerals at elevated temperatures. Appl. Geochem. 93, 190–208.

Weber, J., Barthel, J., Brandt, F., Klinkenberg, M., Breuer, U., Kruth, M., Bosbach, D., 2016. Nano-structural features of barite crystals observed by electron microscopy and atom probe tomography. Chem. Geol. 424, 51–59. https://doi.org/10.1016/j.chemgeo.2016.01.018.

Weber, J., Barthel, J., Klinkenberg, M., Bosbach, D., Kruth, M., Brandt, F., 2017. Retention of ^{226}Ra by barite: the role of internal porosity. Chem. Geol. 466, 722–732.

Weber, J., Bracco, J.N., Poplawsky, J.D., Ievlev, A.V., More, K.L., Lorenz, M., Bertagni, A. L., Jindra, S.A., Starchenko, V., Higgins, S.R., Stack, A.G., 2018. Unraveling the effects of strontium incorporation on barite growth: in situ and ex situ observations using multiscale chemical imaging. Cryst. Growth Des. 18 (9), 5521–5533.

Weber, J., Bracco, J.N., Yuan, K., Starchenko, V., Stack, A.G., 2021. Studies of mineral nucleation and growth across multiple scales: review of the current state of research using the example of Barite (BaSO$_4$). ACS Earth Space Chem. 5 (12), 3338–3361. https://doi.org/10.1021/acsearthspacechem.1c00055.

Weyl, P.K., 1959. Pressure solution and the force of crystallization: a phenomenological theory. J.Geophys. Res. 64 (11), 2001–2025. https://doi.org/10.1029/JZ064i011p02001.

Zhang, Z., Nancollas, G.H., 2014. The influence of pH on barite nucleation and growth. Chem. Eng. Sci. 108, 22–29.